Original Manuscript

SHM Structural Health Monitoring

Structural Health Monitoring
2022, Vol. 0(0) 1–27

DOI: 10.1177/14759217221099967
journals.sagepub.com/home/shm
SAGE

Prediction of frequency and spatially dependent attenuation of guided waves propagating in mounted and unmounted A380 parts made up of anisotropic viscoelastic composite laminates

Shuanglin Guo, Marc Rébillat and Nazih Mechbal

Abstract

Monitoring damage in composite structures using guided wave-based techniques is particularly effective due to their excellent ability to propagate over relatively long distance and hence to cover a large area with few testing time and equipment. The industrialization of this method is highly tributary of the number and placement of the active elements. Yet, the optimal sensorization of a structure relies on the decrease in amplitude of guided waves over propagation distance. A reliable prediction of attenuation of guided waves is still a challenge especially for anisotropic viscoelastic composite materials which exhibit complex changes of attenuation with propagation direction and thus a spatial dependency of attenuation. In this paper, the damped global matrix method (dGMM), having stable and efficient merits, is developed to predict the frequency and spatially dependent attenuation of waves propagating in anisotropic composite materials. dGMM integrates three damping models (Hysteretic, Kelvin-Voigt, and Biot models) into the conventional undamped GMM to consider viscoelasticity of composite laminates. The proposed dGMM is first theoretically validated by numerical comparison with the semi-analytical finite element method. In addition, two industrial case studies, parts of an A380 nacelle at scale one, are employed to experimentally validate the proposed attenuation prediction method. The first one is a fan cowl structure and the second one is an inner fixed structure, both either unmounted or mounted on an actual instrumented A380 plane. This makes the validation extremely valuable for both the scientific and industrial communities. The proposed attenuation prediction method thus paves the way to optimally deploy sensor network for structural health monitoring of anisotropic viscoelastic composite structures.

Keywords

Structural heath monitoring, attenuation of guided waves, anisotropic composite laminates, viscoelastic damping, damped global matrix method, inverse problem

Introduction

For multi-layered composite structures used in aeronautic applications, monitoring their health and integrity over time and under operational conditions is mandatory in order to guarantee safety. When the structure is endowed with embedded sensors, the process is referred to as structural health monitoring (SHM) and is expected to detect and identify structural damage at an early stage to prevent catastrophic failure occurrence.[1,2] Among all kinds of existing SHM techniques, the ultrasonic guided waves strategy is particularly effective for such composite structures because guided waves can propagate over important distances and thus cover a large area with few sensors and few testing times. This benefit results in reduced labor and equipment needed to perform a test and makes long-range inspection possible[3] which makes it easier to overcome certain industrial implementation constraints. When adopting guided waves as an inspection tool for composite structures, the attenuation property of these waves is an

PIMM Laboratory, Arts et Métiers Sciences et Technologies, CNRS, CNAM, HESAM Université, Paris, France

Corresponding author:
Nazih Mechbal, PIMM Laboratory, Arts et Métiers Sciences et Technologies, 151 boulevard de l'Hôpital, Paris 75013, France.
Email: nazih.mechbal@ensam.eu

essential aspect that should be considered carefully in addition to dispersion property.[4] This is especially true for carbon fiber reinforced composites as such materials possess inherent viscoelasticity that causes attenuation and thus impacts significantly the sensor network deployment in terms of sensor geometry, installation, number, and position.[5,6] In comparison with the network used for lightly damped structures, a larger sensor network (i.e., having a larger number of sensors) is required to cover the highly damped structures with enough wave amplitudes.[7,8] Furthermore, attenuation property plays an important role in amplitude-based damage identification methods[9] and machine learning tools for modeling guided waves.[10]

Over the past decades, studies related to attenuation are mainly focused on numerical computations and experimental measurements. In composite structures, material viscoelastic damping, usually characterized by Hysteretic (HR) or Kelvin–Voigt (KV) damping models, is the primary factor that causes attenuation.[11,12] The Rayleigh damping model is also adopted to investigate the damping effect on wave attenuation.[13,14] Theoretically, attenuation coefficients of guided waves can be computed from the corresponding dispersion equations (DEs). Thus, considerable efforts have been made to derive accurate or approximated DEs, being complex-valued in the viscoelastic media, and to develop efficient numerical algorithms to solve them. The simplest one is the classical Rayleigh–Lamb equation which represents wave propagation in a homogeneous isotropic viscoelastic plate.[15,16] The partial wave superposition approach (PWSA) is generally employed to derive the DEs of the single-layer anisotropic viscoelastic plate.[17,18] For the multi-layered system, PWSA is extended to a class of matrix-based methods, for example, transfer matrix method (TMM)[19] and global matrix method (GMM),[20] which are based on the linear 3D elasticity theory and thus become the standard manner to derive the analytical DEs of this system. However, solving these equations is not an easy task and it usually requires Lowe's dual-variable root-finding method[21] or Zhu-Qian's 2D Module Ratio Convergence Method (2D MRCM).[15] Some alternative approaches turn to establish the approximated DEs but are solved by efficient root-searching algorithms such as the Newton–Raphson method and eigenvalue decomposition method. The representatives are the approaches based on Legendre polynomials[22–24] and higher-order plate theory.[25–27] Furthermore, discrete numerical methods are widely applied as well to solve the problem of complex waves in multi-layered viscoelastic plates due to their easy implementation. For instance, one can cite the wave finite element method using the Floquet periodicity condition,[28,29] the spectral collocation method based on Chebyshev polynomials,[30,31] and the semi-analytical finite element method (SAFE) suitable for arbitrary cross-section waveguides.[32–34] The common characteristic of these methods lies in that discretization only takes place in the thickness direction of the plate, thus increasing computational efficiency compared to the traditional 3D finite element modeling. For efficiently simulating transient wave propagation and interaction with structural damage in anisotropic viscoelastic composite structures, the local interaction simulation approach (LISA) has been developed and improved in some references.[35,36]

In addition to the numerical approach, attenuation coefficients can be also measured experimentally, but the related works are scarce compared to the abundant theoretical advancements. The simplest approach consists in computing the attenuation rate of wave amplitudes between two sensors in an A-scan experiment.[7,13] A comprehensive method is to use a curve fitting technique which estimates attenuation by fitting the experimental data of wave amplitudes versus propagation distances, having the merit of considering both geometric spreading and structural damping.[11,37] Besides, two advanced identification methods are also used, including the matrix pencil method[16] and the estimation of signal parameters via rotational invariance techniques.[38] The common characteristic of both methods lies in that they can identify not only the attenuation coefficient but also the propagating wavenumber.

In the aforementioned works, much effort was put to obtain the 3D dispersion curves depending on frequency at a fixed propagation direction.[18,24,31] Scarce work was devoted to study the directional property of attenuation, especially for practical engineering structures, which has a great significance for sensor network operational deployment in anisotropic composite plates. To this end, this paper proposes a new method to predict the frequency and spatially dependent attenuation of guided waves propagating in anisotropic viscoelastic composite laminates. Here *frequency* and *spatially* means that wave attenuation depends not only on frequency but also on the propagation direction. The proposed method extends the conventional damping-free GMM to the damping case by incorporating viscoelastic damping models. This method is termed "dGMM" for the damped global matrix method. It is supported by a two-step numerical root-solving algorithm, having stable and efficient merits. The proposed dGMM is first verified theoretically by numerical comparison with the SAFE method, then validated through experimentation on two aeronautic composite parts (at scale one) of an Airbus A380 nacelle as shown in Figure 1. For each structure, two cases were considered, unmounted and mounted parts on the plane. The two structures are rather different as one is made up of a multi-layered carbon epoxy composite plate with many stiffeners, fan cowl structure (FCS) as shown in Figure 1(a), which is 2.20 m high and 5.80 m in half-circumference; and the other one is a sandwich-type structure, inner fixed structure (IFS) shown in Figure 1(b), with an aluminum alloy honeycomb core and

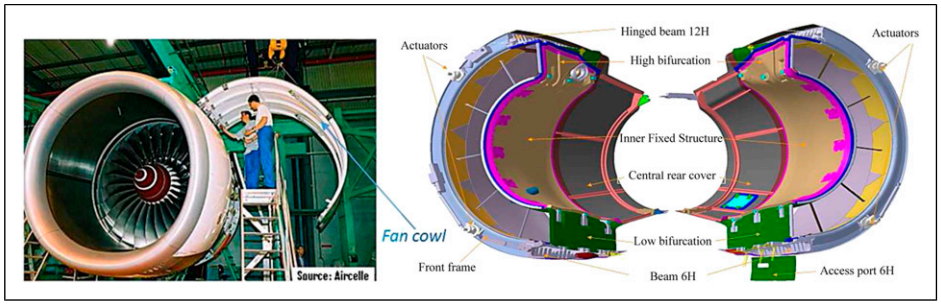

Figure 1. The studied aircraft nacelles of an A380 plane for (a) fan cowl structure and (b) inner fixed structure.

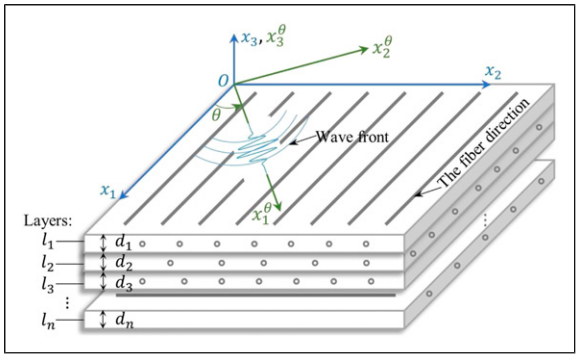

Figure 2. Schematical diagram of an *n*-layered aeronautic composite laminate.

two multi-ply carbon epoxy outer skins, which has a dimension of 2.75 m in height and 3.80 m in half-circumference.[39] It should be emphasized here, that unlike the experiments on small-scale plates,[5–7,13,34] the results reported in this paper are the unique work so far concerning attenuation prediction for practical aeronautic structures, and the most important contribution to the state-of-the-art is that in-service data of the mounted cases of both structures are used to validate the proposed method.

This paper is organized as follows: the framework of dGMM is derived in the second section; the attenuation identification process and viscoelastic material properties estimation process are introduced in the third section; the two case studies on FCS and IFS are presented in the fourth and fifth section, respectively; discussion and future work are given in the sixth section; finally, the last section draws the conclusion.

Wave propagation theory in the viscoelastic composite laminate

Aeronautic composite structures are generally designed as multi-layered laminates as schematically shown in Figure 2. The materials composing the laminate have intrinsic viscoelastic damping properties that cause attenuation of guided waves during propagation. To this end, the damping models that will be considered are first introduced.

Viscoelastic damping models of composite materials

The HR and KV models are two common damping models able to describe the viscoelasticity of composite materials[40] as presented in equations (1) and (2), respectively. For both models, the elastic modulus is considered as a complex number E^*, in which the real part E is the storage modulus and the imaginary part is associated with two factors γ_{HR} and γ_{KV} that are defined as the respective loss factors of the two models. Besides, a less common damping model named Biot (BT) model is presented in equation (3), which is mainly applied to highly damped aerospace structures.[41] Amongst the three models, the HR model generates a complex modulus E^* independent of frequency ω, whereas KV and BT models produce a frequency-dependent complex modulus. Thus, the dependency property on ω is attached to E^* for the two models, that is, $E^*(\omega)$

$$E^* = E(1 - \mathrm{i}\gamma_{HR}) \quad \text{HR model} \tag{1}$$

$$E^*(\omega) = E\left(1 - \mathrm{i}\gamma_{KV}\frac{\omega}{\omega_c}\right) \quad \text{KV model} \tag{2}$$

$$E^*(\omega) = E\left[1 + \frac{2}{\pi}\gamma_{BT}\ln\sqrt{1 + \left(\frac{\omega}{\epsilon}\right)^2} - \mathrm{i}\frac{2}{\pi}\gamma_{BT}\arctan\left(\frac{\omega}{\epsilon}\right)\right] \quad \text{BT model} \tag{3}$$

where "i" is the unit of the imaginary number and the superscript "*" denotes that the associated term belongs to the complex number family; ω_c is the characteristic frequency of the KV model characterizing that γ_{KV} is measured at ω_c; γ_{BT} and ϵ are the loss factor and scaling factor of the BT model, respectively.

For a general layer composing the laminate, for example, layer l_1 in Figure 2, the stress-strain relation of this layer is characterized by nine independent elastic constants, that is., three longitudinal moduli E_1, E_2, and E_3, and three shear moduli G_{23}, G_{31}, and G_{12}, as well as three Poisson's ratios v_{12}, v_{13}, and v_{23}. Since the viscoelastic property of composite materials is considered in this paper, a given damping model selected among equations (1) and (2) or (3) can be applied to the six elastic moduli, thus producing frequency-dependent complex moduli[28] $E_1^*(\omega)$ $E_2^*(\omega)$, $E_3^*(\omega)$, $G_{23}^*(\omega)$, $G_{31}^*(\omega)$, $G_{12}^*(\omega)$.[1] In view of this, the usual stiffness matrix $\mathbf{C}$ becomes correspondingly a frequency-dependent complex matrix $\mathbf{C}^*(\omega)$ as presented in equation (4), which shows the orthotropic anisotropy of composite materials

$$\mathbf{C}^*(\omega) = \begin{bmatrix} \frac{1}{E_1^*(\omega)} & \frac{-v_{12}}{E_1^*(\omega)} & \frac{-v_{13}}{E_1^*(\omega)} & 0 & 0 & 0 \\ \frac{-v_{21}}{E_2^*(\omega)} & \frac{1}{E_2^*(\omega)} & \frac{-v_{23}}{E_2^*(\omega)} & 0 & 0 & 0 \\ \frac{-v_{31}}{E_3^*(\omega)} & \frac{-v_{32}}{E_3^*(\omega)} & \frac{1}{E_3^*(\omega)} & 0 & 0 & 0 \\ 0 & 0 & 0 & \frac{1}{G_{23}^*(\omega)} & 0 & 0 \\ 0 & 0 & 0 & 0 & \frac{1}{G_{31}^*(\omega)} & 0 \\ 0 & 0 & 0 & 0 & 0 & \frac{1}{G_{12}^*(\omega)} \end{bmatrix}^{-1} \tag{4}$$

where the six Poisson's ratios are real numbers and v_{21}, v_{31}, and v_{32} are not independent due to the symmetry of the stiffness matrix.

The stiffness matrix $\mathbf{C}^*(\omega)$ corresponds to each layer's fiber direction, for instance, the x_1 axis direction in the layer l_1 of Figure 2. It should be rotated to the wave propagation direction that is along the x_1^θ axis as shown in Figure 2, in order to ease the following derivations. This can be done through tensor operations. Firstly, each coefficients $C_{pq}^*(\omega)$ in equation (4) can be transformed into the coefficients of the fourth rank tensor $c_{ijkl}^*(\omega)$ via the Voigt notation with the one-to-one correspondence ij or kl =11, 22, 33, 23(32), 13(31), 12(21) $\leftrightarrow p$ or q =1, 2, 3, 4, 5, 6. Then, the stiffness tensor $c_{ijkl}^*(\omega)$ are rotated to the wave propagation direction based on the tensor rotation rule as presented in equation (5), in which the Einstein summation convention is implied for repeated index[40]

$$c_{mnop}^*(\omega,\theta) = R_{mi}(\theta)R_{nj}(\theta)R_{ok}(\theta)R_{pl}(\theta)c_{ijkl}^*(\omega) \tag{5}$$

Here, $c_{mnop}^*(\omega,\theta)$ represents the rotated stiffness tensor and $R_{mi}(\theta)$ the coefficients of the rotation tensor as presented in equation (6)

$$\mathbf{R}(\theta) = \begin{bmatrix} \cos(\theta) & \sin(\theta) & 0 \\ -\sin(\theta) & \cos(\theta) & 0 \\ 0 & 0 & 1 \end{bmatrix} \tag{6}$$

with θ positive when the rotation is along the counterclockwise direction.

Finally, the tensor form stiffness $c_{mnop}^*(\omega,\theta)$ is transformed back to the matrix form $C_{pq}^*(\omega,\theta)$ via Voigt notation, as expanded in equation (7), which shows the monoclinic anisotropy of composite materials

$$\mathbf{C}^*(\omega,\theta) = \begin{bmatrix} C_{11}^* & C_{12}^* & C_{13}^* & 0 & 0 & C_{16}^* \\ & C_{22}^* & C_{23}^* & 0 & 0 & C_{26}^* \\ & & C_{33}^* & 0 & 0 & C_{36}^* \\ & & & C_{44}^* & C_{45}^* & 0 \\ & \text{sym} & & & C_{55}^* & 0 \\ & & & & 0 & C_{66}^* \end{bmatrix} \tag{7}$$

Damped global matrix method

When guided waves propagate in a general layer l_i, the displacement and stress vectors can be expressed as a compact form in equations (8) and (9) that represent the superposition of six partial waves derived from 3D elasticity theory[42]

$$\mathbf{u}^{l_i} = [u_1,u_2,u_3]^{\mathrm{T}} = \boldsymbol{\Upsilon}^{l_i}\boldsymbol{\Lambda}^{l_i}(x_3)\boldsymbol{\eta}^{l_i}\mathrm{e}^{\mathrm{i}k(x_1-vt)} \tag{8}$$

$$\boldsymbol{\sigma}^{l_i} = [\sigma_{33},\sigma_{23},\sigma_{13}]^{\mathrm{T}} = \mathrm{i}k\boldsymbol{\beta}^{l_i}\boldsymbol{\Lambda}^{l_i}(x_3)\boldsymbol{\eta}^{l_i}\mathrm{e}^{\mathrm{i}k(x_1-vt)} \tag{9}$$

where the superscript "l_i" implies that the associated term belongs to the layer l_i. $\boldsymbol{\Upsilon}^{l_i}$ and $\boldsymbol{\beta}^{l_i}$ are the amplitude matrix of displacement and stress, respectively. $\boldsymbol{\Lambda}^{l_i}(x_3)$ is a diagonal matrix depending on the thickness direction coordinate x_3. $\boldsymbol{\eta}^{l_i}$ is the partial wave participation vector. They are uniformly defined in equation (10). Besides, k and v are the wavenumber and phase velocity,

respectively, and they are related with frequency through $\omega = kv$

$$\boldsymbol{\Upsilon}^{l_i} = \begin{bmatrix} 1 & 1 & 1 & 1 & 1 & 1 \\ V_1 & V_2 & V_3 & V_4 & V_5 & V_6 \\ W_1 & W_2 & W_3 & W_4 & W_5 & W_6 \end{bmatrix}$$
$$\boldsymbol{\beta}^{l_i} = \begin{bmatrix} \beta_{11} & \beta_{12} & \beta_{13} & \beta_{14} & \beta_{15} & \beta_{16} \\ \beta_{21} & \beta_{22} & \beta_{23} & \beta_{24} & \beta_{25} & \beta_{26} \\ \beta_{31} & \beta_{32} & \beta_{33} & \beta_{34} & \beta_{35} & \beta_{36} \end{bmatrix} \quad (10)$$
$$\boldsymbol{\Lambda}^{l_i}(x_3) = \begin{bmatrix} \mathrm{e}^{\mathrm{i}k\alpha_1 x_3} & & \\ & \ddots & \\ & & \mathrm{e}^{\mathrm{i}k\alpha_6 x_3} \end{bmatrix}$$
$$\boldsymbol{\eta}^{l_i} = [\eta_1, \eta_2, \eta_3, \eta_4, \eta_5, \eta_6]^{\mathrm{T}}$$

In equation (10), α_j, V_j and W_j with $(j = 1,\ldots,6)$ are computed from the Christoffel equation, equation (11), that is, the non-trivial vector $[U,V,W]^{\mathrm{T}}$ requires the singularity of the coefficient matrix in equation (11), which further

$$\begin{bmatrix} \left(C_{11}^* - \rho v^2 + C_{55}^* \alpha^2\right) & \left(C_{16}^* + C_{45}^* \alpha^2\right) & \left(C_{13}^* + C_{55}^*\right)\alpha \\ \left(C_{16}^* + C_{45}^* \alpha^2\right) & \left(C_{66}^* - \rho v^2 + C_{44}^* \alpha^2\right) & \left(C_{36}^* + C_{45}^*\right)\alpha \\ \left(C_{13}^* + C_{55}^*\right)\alpha & \left(C_{36}^* + C_{45}^*\right)\alpha & \left(C_{55}^* - \rho v^2 + C_{33}^* \alpha^2\right) \end{bmatrix} \begin{bmatrix} U \\ V \\ W \end{bmatrix} = \begin{bmatrix} 0 \\ 0 \\ 0 \end{bmatrix} \quad (11)$$

leads to a cubic equation in terms of α^2 as presented in equation (12)

$$A_6\alpha^6 + A_4\alpha^4 + A_2\alpha^2 + A_0 = 0 \quad (12)$$

where the four polynomial coefficients are presented in Appendix 1 for convenience. For each solution of α_j in equation (12), there corresponds a pair of solutions of V_j, W_j, β_{1j}, β_{2j}, β_{3j} as presented in equations (13) and (14)

$$\begin{cases} V_j = \dfrac{\left(C_{11}^* - \rho v^2 + C_{55}^* \alpha_j^2\right)\left(C_{36}^* + C_{45}^*\right) - \left(C_{16}^* + C_{45}^* \alpha_j^2\right)\left(C_{13}^* + C_{55}^*\right)}{\left(C_{13}^* + C_{55}^*\right)\left(C_{66}^* - \rho v^2 + C_{44}^* \alpha_j^2\right) - \left(C_{16}^* + C_{45}^* \alpha_j^2\right)\left(C_{36}^* + C_{45}^*\right)} \\ W_j = \dfrac{\left(C_{11}^* - \rho v^2 + C_{55}^* \alpha_j^2\right)\left(C_{36}^* + C_{45}^*\right)\alpha_j - \left(C_{16}^* + C_{45}^* \alpha_j^2\right)\left(C_{13}^* + C_{55}^*\right)\alpha_j}{\left(C_{16}^* + C_{45}^* \alpha_j^2\right)\left(C_{55}^* - \rho v^2 + C_{33}^* \alpha_j^2\right) - \left(C_{13}^* + C_{55}^*\right)\left(C_{36}^* + C_{45}^*\right)\alpha_j^2} \end{cases} (j = 1,\ldots,6) \quad (13)$$

$$\begin{cases} \beta_{1j} = C_{13}^* + C_{36}^* V_j + C_{33}^* \alpha_j W_j \\ \beta_{2j} = C_{45}^* \alpha_j + C_{44}^* \alpha_j V_j + C_{45}^* W_j \\ \beta_{3j} = C_{55}^* \alpha_j + C_{45}^* \alpha_j V_j + C_{55}^* W_j \end{cases} (j = 1,\ldots,6) \quad (14)$$

To this step, the displacement and stress vectors in equations (8) and (9) can be combined to ease the application of the continuity condition at the interface of inter-lamination. We then have equation (15)

$$\mathbf{S}^{l_i} = \begin{bmatrix} \mathbf{u}^{l_i} \\ \boldsymbol{\sigma}^{l_i} \end{bmatrix} = \begin{bmatrix} \boldsymbol{\Upsilon}^{l_i} \\ \mathrm{i}k\boldsymbol{\beta}^{l_i} \end{bmatrix} \boldsymbol{\Lambda}^{l_i}(x_3)\boldsymbol{\eta}^{l_i}\mathrm{e}^{\mathrm{i}k(x_1 - vt)} = \mathbf{Z}^{l_i}(x_3)\boldsymbol{\eta}^{l_i}\mathrm{e}^{\mathrm{i}k(x_1 - vt)} \quad (15)$$

where $\mathbf{Z}^{l_i}(x_3) = \begin{bmatrix} \boldsymbol{\Upsilon}^{l_i} \\ \mathrm{i}k\boldsymbol{\beta}^{l_i} \end{bmatrix} \boldsymbol{\Lambda}^{l_i}(x_3)$. At the interface between layers l_i and l_{i+1}, the continuity condition requires that the displacement and stress fields should be continuous, as stated in equation (16). Besides, the traction-free boundary condition at the two outer surfaces should be satisfied due to the free surface of the plate, as expressed in equation (17)

$$\mathbf{S}^{l_i}\big|_{x_3 = d_i} = \mathbf{S}^{l_{i+1}}\big|_{x_3 = 0} \quad (i = 1,\cdots,n-1) \quad (16)$$

$$\boldsymbol{\sigma}^{l_1}\big|_{x_3 = 0} = 0 \quad \text{and} \quad \boldsymbol{\sigma}^{l_n}\big|_{x_3 = d_n} = 0 \quad (17)$$

For the n-layered laminate system shown in Figure 2, the continuity condition of each interface can be consistently

assembled to form a global matrix system, as presented in equation (18), in which the subscript "4:6" in $\mathbf{Z}^{l_1}(0)$ and $\mathbf{Z}^{l_n}(d_n)$ means that only the fourth to sixth rows of the two matrices are evaluated because these rows correspond to stress terms σ_{33}, σ_{23}, and σ_{13} and thus represent the traction-free boundary conditions in equation (17)

$$\begin{bmatrix} -\mathbf{Z}^{l_1}_{4:6}(0) & & & & & \\ \mathbf{Z}^{l_1}(d_1) & -\mathbf{Z}^{l_2}(0) & & & & \\ & \ddots & \ddots & & & \\ & & & \mathbf{Z}^{l_i}(d_i) & -\mathbf{Z}^{l_{i+1}}(0) & \\ & & & & \ddots & \\ & & & & \mathbf{Z}^{l_{n-1}}(d_{n-1}) & -\mathbf{Z}^{l_n}(0) \\ & & & & & \mathbf{Z}^{l_n}_{4:6}(d_n) \end{bmatrix} \begin{bmatrix} \boldsymbol{\eta}^{l_1} \\ \vdots \\ \boldsymbol{\eta}^{l_i} \\ \boldsymbol{\eta}^{l_{i+1}} \\ \vdots \\ \boldsymbol{\eta}^{l_n} \end{bmatrix} = \begin{bmatrix} 0 \\ \vdots \\ 0 \\ 0 \\ \vdots \\ 0 \end{bmatrix} \tag{18}$$

The huge global matrix in equation (18) can be concisely rewritten as $\mathbf{G}(\omega,k^*,\theta) \in \mathbb{C}^{6n\times 6n}$ given that this matrix depends on frequency ω, wavenumber k, and propagation angle θ on the one hand, and on the other hand, k should be a complex number, that is, k^*,[2] owing to the effect of viscoelastic damping introduced from the stiffness matrix in equation (4). The non-trivial solution of $\boldsymbol{\eta}^{l_i}$ in equation (18) requires that the determinant of the global matrix $\mathbf{G}(\omega,k^*,\theta)$ should vanish, which finally generates the DE of the n-layered laminate system, as presented in equation (19)

$$\mathfrak{D}\left(\omega,k^*,\theta\right) = \det\left\{\mathbf{G}\left(\omega,k^*,\theta\right)\right\} = 0 \tag{19}$$

where $k^* = k_r + \mathrm{i}k_i$. Both k_r and k_i are real positive numbers, and k_r is the wave's propagating wavenumber and k_i the attenuation coefficient given in Nepers per meter, Np/m (1 Np/m=8.69 dB/m).[40]

Equation (19) is a nonlinear transcendental equation with complex, multivariate, and multi-roots characteristics. Solving this equation is mathematically intractable. We will present and implement in detail an original solving algorithm in the subsequent section. Thus, once the solutions of equation (19) are obtained, the corresponding solutions of $\boldsymbol{\eta}^{l_i}$ in equation (18) can be extracted from the zero-eigenvalue correlated eigenvectors of the global matrix $\mathbf{G}(\omega,k^*,\theta)$. Finally, the displacement and stress mode shapes of the laminate can be portrayed along the plate thickness direction through equations (8) and (9). For some composite aeronautic laminates that have symmetry in terms of stacking sequence, the solution points (ω,k^*,θ) in equation (19) can be further classified into symmetric and anti-symmetric modes by checking the symmetry condition[42] of the computed displacement and stress mode shapes at the midplane of the whole laminate, as presented in equation (20)

$$\begin{cases} [u_3,\sigma_{23},\sigma_{13}]_{\text{midplane}} = [0,0,0] & \text{symmetric modes} \\ [u_1,u_2,\sigma_{33}]_{\text{midplane}} = [0,0,0] & \text{anti}-\text{symmetric modes} \end{cases} \tag{20}$$

With the solved dispersion relation between ω and k^* at a specified θ_0, phase velocity c_p is computed from equation (21). If the damping effect is slight, that is, $k_i \ll k_r$, meanwhile if the structure is quasi-isotropic, group velocity c_g can be computed through equation (22), which is an isotropic model. If necessary, for pure anisotropic structures, the exact anisotropic model studied in Ref. 43 can be used to compute group velocity. But for heavily damped structures, the energy velocity c_e defined in equation (23) should be adopted because in this case, the imaginary part k_i is large enough such that the group velocity computed through equation (22) is physically meaningless[17,44]

$$c_p = \frac{\omega}{k_r} \tag{21}$$

$$c_g = \frac{\partial\omega}{\partial k_r} \tag{22}$$

$$c_e = \frac{\int_0^H \langle P_1\rangle \mathrm{d}x_3}{\int_0^H \left(\langle E_k\rangle + \langle E_p\rangle\right)\mathrm{d}x_3} \tag{23}$$

where H is the plate's total thickness, $\langle P_1\rangle$ is the time-averaged *Poynting* vector along the wave propagation direction, that is, x_1^θ shown in Figure 2, and $\langle E_k\rangle$ and $\langle E_p\rangle$ are

the time-averaged kinetic and potential energy density stored in the waveguide. The three terms are defined in equation (24), in which the Einstein summation convention is implied for repeated index

$$\langle P_i\rangle = -\frac{1}{2}\mathrm{Re}\{\sigma_{ij}\bar{\dot{u}}_j\}(i=1,2,3),$$
$$\langle E_k\rangle = \frac{1}{4}\mathrm{Re}\{\rho\dot{u}_i\bar{\dot{u}}_i\},\langle E_p\rangle = \frac{1}{4}\mathrm{Re}\left\{\sigma_{ij}\bar{\varepsilon}_{ij}\right\} \quad (24)$$

where $\mathrm{Re}\{\cdot\}$ is the real part operator, $\dot{u}_i$ is the particle velocity of the waveguide along direction x_i^{θ}, and the overbar "–" denotes the complex conjugate.

Numerical algorithm of solving the complex dispersion equation

The task of solving the complex DE, equation (19) is extremely complex from mathematical view. Indeed, it is a multivariate transcendental equation given that, at a specified propagation angle θ_0, for a solution pair (ω,k^*) there are actually three real variables (ω,k_r,k_i) to be identified because of $k^* = k_r + \mathrm{i}k_i$. Thus, a certain dimensionality reduction is necessary in order to solve the ternary-variable equation. Note that the complex stiffness matrix $\mathbf{C}^*(\omega)$ is frequency-dependent as implied by equation (4), thus, ω should be considered as another independent variable in addition to θ during the solving process. Specifically, at a specified propagation angle θ_0, ω is independently fixed as a constant ω_0, by doing so, the original quaternary-variable equation $\mathfrak{D}(\omega,k_r,k_i,\theta) = 0$ is now transited to a dual-variable equation $\mathfrak{D}(k_r,k_i;\omega_0,\theta_0) = 0$. This equation can be solved by applying a dual-variable searching method.[21] In this paper, a recently developed method named 2D MRCM[15] is employed which mathematically transforms the dual-variable root-finding process to search the global minimal modulus of the characteristic function $|\mathfrak{D}(k_r,k_i)|$ by checking the module ratio convergence. The interested readers can refer to Zhu's works[15,18] for more information. To get the full-frequency spectrum of k_r and k_i, the above solving process is repeated by changing ω_0, which reveals the dispersion property of both quantities. Alternatively, by changing θ_0, the resulted diagrams are the polar plot of k_r and k_i, which just shows the anisotropic property of guided waves propagating in anisotropic composite laminates, viz. the spatial effect.

It is well known that there are multiple solutions (k_r,k_i) at a stationary pair (ω_0,θ_0), which represents multiple guided wave modes propagations at the specified frequency ω_0. 2D MRCM can search all the solutions by scanning the structured grids as long as the step length of the scanning element is small enough. Scanning the whole space of interest is required to generate the multi-modal 3D dispersion curves (k_r,k_i,ω), known as the forward procedure, but is time-consuming. If only a single mode's dispersion curve is desired, for example, S0 or A0 mode, a single curve tracing technique can accelerate the searching efficiency since tracing the trajectory of a single mode's solution is just a fractional workload of searching the full 3D spectral lines. In addition, in the following inverse procedure of the model updating process, the traced single mode's dispersion curve can be immediately contrasted to the counterpart that is experimentally measured, thereof avoiding the branch identification and mode matching problem.[45] To this end, a quadratic extrapolation-based single-mode curve tracing technique is developed, as schematically illustrated in Figure 3. It is detailed in the following paragraph.

Specifically, for the nth $(n\geq 4)$ solution k_n^* of a certain mode to be solved at the specified ω_n, once the previous three solution points (ω_{n-1},k_{n-1}^*), (ω_{n-2},k_{n-2}^*) and (ω_{n-3},k_{n-3}^*) in the curve are known, the initial guess $k_n^{'*}$ is calculated by extrapolating the three points to ω_n. Then, the accurate solution k_n^* is searched via 2D MRCM in the vicinity of the guess $k_n^{'*}$. For the first three solution points (ω_1,k_1^*), (ω_2,k_2^*) and (ω_3,k_3^*), they are searched via 2D MRCM in the vicinity of the guesses $k_1 + \mathrm{i}0$, $k_2 + \mathrm{i}0$ and $k_3 + \mathrm{i}0$, where k_1, k_2, k_3 are the solutions of the real case DE, that is, undamped case, at frequencies ω_1, ω_2, ω_3, which is an easy task. This strategy is particularly effective for tracing fundamental modes' curves, that is, S0, A0, and SH0 modes, since the proximity of the complex case curve to the real case one in $\omega - k_r$ plane guarantees the success of the tracing process, as illustrated in Figure 3. It is worth noting that the extrapolation equation $k_{r,n}^{'}$ in Figure 3, which is the real part of $k_n^{'*}$, can be applied to non-constant frequency increment given that the frequency increment obtained from the real case solution may not be equal to the one of the complex case.

The above elaboration is now implemented to be a two-step dGMM algorithm of solving the complex DE as presented in Figure 4. Step 1 is trivial because it works out the real case DEs through the undamped GMM.[42] Step 2 is just the realization of the combined dGMM, curve tracing technique, and 2D MRCM.

Data-driven structural parameter estimation

The key to success of predicting attenuation using the developed algorithm in Figure 4 relies on the accuracy of the viscoelastic loss factors that are involved in the damping models in equations (1), (2), and (3). These parameters can be obtained from the material manufacturer or from standard

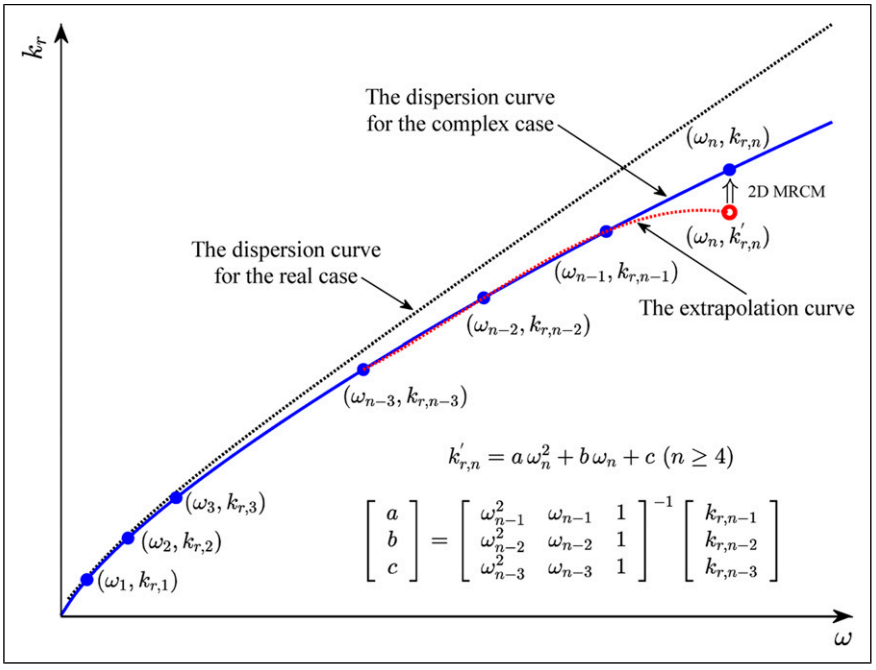

Figure 3. The schematic diagram of the curve tracing technique.

mechanical test data.[46,47] However, in most cases, both ways are not available, especially for *in-situ* structures which are under service. On the other hand, the acquired guided wave signals from the installed sensor network contain fruitful information of the monitored structures, including the materials' properties of interest. In this paper, an original model updating procedure is proposed to estimate the material loss factors of damping models, which is an inverse process in contrast with the forward dispersion curves computations based on known material parameters.[18,22]

Identification of attenuation coefficient

For circular-like crested guided waves propagating in composite plates, geometric spreading and material damping are two main factors of wave amplitude attenuation.[11] The former is responsible for the near-field propagation (usually less than three wavelengths) and the latter mainly for far-field propagation.[11,48] In equation (8), the effect of geometric spreading is not accounted since it is a solution of the plate's free vibration,[42] in other words, far-field condition is fulfilled. As such, the displacement field of equation (8) for a general layer l_i can be extended to the whole laminate system, as expressed in equation (25)

$$u_i(x_1,x_3,t) = \widehat{u}_i(x_3)\mathrm{e}^{\mathrm{i}(k^* x_1 - \omega t)} \quad (i = 1,2,3) \tag{25}$$

where $\widehat{u}_i(x_3)$ is the through thickness wave amplitude at the excitation source. Substituting $k^* = k_r + \mathrm{i}k_i$ into equation (25) leads to equation (26)

$$u_i(x_1,x_3,t) = \widehat{u}_i(x_3)\mathrm{e}^{-k_i x_1}\mathrm{e}^{\mathrm{i}(k_r x_1 - \omega t)} (i = 1,2,3) \tag{26}$$

Comparing the two equations, the wave amplitude decays exponentially over propagation distance x_1 with decaying ratio k_i, which allows to interpret the physical essence of the imaginary part of the complex wavenumber, that is, being the attenuation coefficient. Besides, equation (26) also demonstrates that all layers share the same attenuation coefficient[3] since the decaying term $\mathrm{e}^{-k_i x_1}$ is independent of the thickness direction coordinate x_3, and it can be measured by the piezoelectric transducers (PZTs) surface mounted on the laminate. Explicitly, making $x_3 = 0$ and taking logarithm for both sides of equation (26) but omitting the phase term $\mathrm{e}^{\mathrm{i}(k_r x_1 - \omega t)}$, a linear formulation is yielded in equation (27)

$$\mathrm{Log}[u_i(x_1,0)] = -k_i x_1 + \mathrm{Log}\left[\widehat{u}_i(0)\right] \quad (i = 1,2,3) \tag{27}$$

where $u_i(x_1,0)$ represents the wave packet amplitude recorded by PZT that is surface mounted at distance x_1 from the excitation source located at 0. Based on equation (27), the attenuation coefficient k_i can be identified from recorded wave signals by linearly regressing logarithmic amplitude of wave packets versus propagation distance x_1, from which the negative of the slope of the regressed line is just the attenuation coefficient.

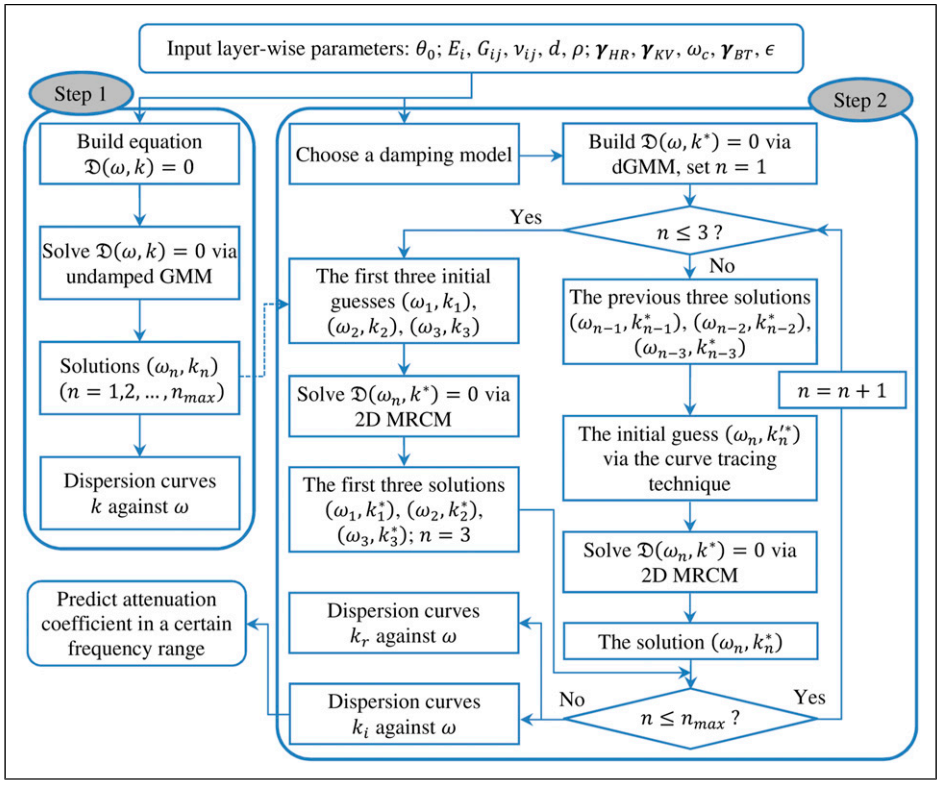

Figure 4. The flowchart of the two-step damped global matrix method algorithm for solving the complex dispersion equations.

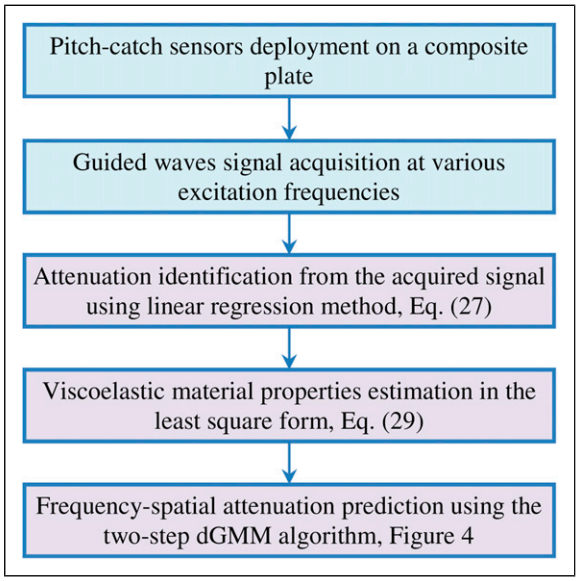

Figure 5. Overview of the proposed method to predict guided waves attenuation.

The linear regression (LR) method is also used to identify energy velocity from the recorded wave signals since at a specified frequency and along a fixed direction, a certain mode's wave packet propagates with a constant velocity value. The detailed manipulation will be presented in the case study sections.

Estimation of viscoelastic loss factors

The experimentally identified attenuation coefficients can be used to estimate the viscoelastic loss factors which are not available in most cases. To this end, the attenuation coefficient k_i is expressed as the function of frequency ω with undetermined loss factors $\boldsymbol{\gamma}$

$$k_i = \mathcal{K}(\boldsymbol{\gamma}, \omega) \tag{28}$$

where $\boldsymbol{\gamma} = [\gamma_1, \gamma_2, \gamma_3, \gamma_{23}, \gamma_{31}, \gamma_{12}]$ in which the six elements are the loss factors of E^*_1, E^*_2, E^*_3, G^*_{23}, G^*_{31}, and G^*_{12}, respectively, as defined in equation (4). When computing, $\boldsymbol{\gamma}$ is specialized to a certain damping model, as defined in equations (1)–(3), $\boldsymbol{\gamma}_{HR}$, $\boldsymbol{\gamma}_{KV}$, and $\boldsymbol{\gamma}_{BT}$. The loss factors $\boldsymbol{\gamma}$ are then determined in the least square sense by inverting the experimentally identified attenuation coefficients, also known as the model updating process (we use here the *lsqcurvefit.m* MATLAB function)

$$\widehat{\boldsymbol{\gamma}} = \arg\min_{\boldsymbol{\gamma}} \sum\nolimits_{l=1}^{m} \left[\mathcal{K}(\boldsymbol{\gamma}, \omega_l) - \tilde{k}_{i,l}\right]^2 \tag{29}$$

where the series pair $(\omega_l, \tilde{k}_{i,l})_{l=1,\cdots,m}$ is the experimentally identified attenuation coefficients at various frequencies,

Table 1. Elastic and viscoelastic material properties of composite lamina of the unmounted fan cowl structure.

(E_1,E_2,E_3) (GPa)	(G_{23},G_{31},G_{12}) (GPa)	$(\nu_{12},\nu_{13},\nu_{23})$	ρ (kg/m^3)	Ply thickness (mm)	Stacking sequence
(60,40,8.1)	(4.8,4.8,4.8)	(0.03,0.3,0.3)	1554	0.28	[0/−45/+45/0]
Hysteretic model	γ_1 = 1.74%, γ_2 = 0.01%, γ_3 = 0.01%, $\gamma_{23},\gamma_{31},\gamma_{12}$ = 0.01%				
Kelvin–Voigt model	γ_1 = 3.47%, γ_2 = 0.01%, γ_3 = 0.012%, $\gamma_{23},\gamma_{31},\gamma_{12}$ = 0.01%, f_c = 250 kHz				

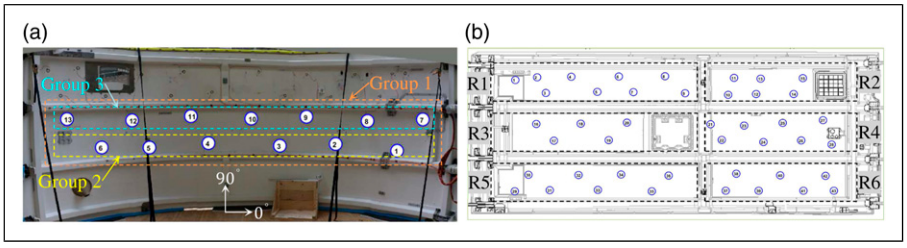

Figure 6. The piezoelectric transducers deployments of fan cowl structure for (a) the unmounted case and (b) the mounted case on an instrumented A380 plane.

and $\hat{\boldsymbol{\gamma}}$ is the estimated loss factors for a certain damping model.

It is worth noting that the function $k_i = \mathcal{K}(\boldsymbol{\gamma},\omega)$ in equation (28) should represent the same branch of dispersion curves as the experimentally identified one, which is achieved through the single-mode curve tracing technique illustrated in Figure 3. In some cases, due to the inaccurate elastic moduli or the existence of uncertainties, the computed energy velocities do not match well with the identified ones. To solve this issue, the same updating process is applied to the experimentally identified energy velocities to calibrate the inaccurate elastic moduli. For brevity, detailed formulation is not presented here but an example is provided in the IFS case study.

Overview of the attenuation prediction method

Once all the required material parameters are available, the numerical dGMM algorithm in Figure 4 is driven to predict various spectra of attenuation including dispersion curves and spatial attenuation distribution. Figure 5 just outlines the overview of the proposed attenuation prediction method in which the three purple boxes summarize the theoretical works established in the previous sections.

Case study on an unmounted and mounted fan cowl structure of A380 plane

Experimental setup

In this section, two cases of FCS, either unmounted or mounted on an instrumented A380 plane, are employed to validate the proposed guided wave attenuation prediction method. The actual FCS is shown in Figure 1(a). This structure is made up of a four-layered carbon epoxy composite plate with stacking sequence [0/−45/+45/0]. The elastic material properties of each layer can be obtained from Fendzi's PhD thesis[39] and listed in Table 1 for convenience, but the viscoelastic properties are not available. Thus, the model updating process introduced previously will be adopted to estimate them. Obtained results are listed in Table 1 for HR and KV models beforehand.

The PZT deployments for both cases are shown in Figure 6. The PZT wafer is made up of Noliac piezoceramic material NCE51, whose material properties are provided in Ref. 49. There are in total 13 and 43 sensors surface installed on the unmounted and mounted FCS, respectively. Due to the presence of stiffeners, the 43 sensors in the mounted FCS are partitioned to six regions, marked from R1 to R6, according to their geometrical characteristics, as shown in Figure 6(b). By doing so, each region can be considered at once and signals are processed with great convenience. The 13 sensors in the unmounted FCS constitute only one region and are thus not marked for brevity. Furthermore, sensors of each region in both cases are intentionally divided into three groups during signal processing according to their alignment pattern, that is, according to their direction with respect to the ply sequence. The group information of the unmounted FCS is illustrated in Figure 6(a). For the mounted FCS, in each region, Group 1 includes all sensors, and Group 2 and 3 contain sensors roughly aligned along the upper and lower horizontal line, respectively. For example, in R1, Group 1 includes sensors from 1 to 9, and Group 2 and 3 include sensors 1, 2, 4, 6, 8 and 3, 5, 7, 9, respectively. The accurate fiber orientation of each layer in the plate is not available but the horizontal direction of the plate is assumed to be the fiber orientation of the 0° layer because this direction leads to the best match between

theoretical predictions and experimental measurements for both energy velocity and attenuation coefficient as will be shown later.

The experimental setup of the unmounted FCS is shown in Figure 7. During testing, the signal generator produced a five-cycle sinusoid tone burst signal modulated by the Hanning window given that this kind of exciting signal becomes a standard in SHM of composite structures.[2] The central frequency of the excitation signal was swept from 50 kHz to 150 kHz with 5 kHz increment for the unmounted FCS experiment whereas for the mounted FCS experiment only measurements performed at 100 kHz are available. The sampling frequency was set as 1 MHz which meets the requirement of the Nyquist sampling theorem. Among these PZT sensors, each one was used as an actuator in a round-robin fashion and the remaining others were receivers, that is, a sequential pitch-catch testing scheme was conducted. The acquired wave signals were processed with time averaging and wavelet denoising to enhance signal-to-noise ratio.[50] Note that the frequency sweep testing is required for understanding the mechanism of wave attenuation within an interested frequency range and it is different from a single sweet spot frequency testing which is desired for damage detection.[51]

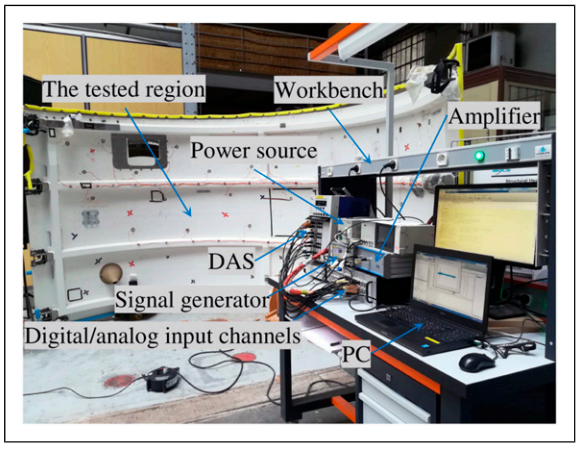

Figure 7. The experimental setup of the unmounted fan cowl structure.

Figure 8(a) shows several typical guided wave signals in Group 2 of the unmounted FCS in which PZT 1 serves as the actuator and its signal is normalized to the same order of magnitude with the receivers. Evidently, the signal amplitude decreases with the increasing propagation distance. Besides, only the S0 mode wave packet is discernible. To examine why the A0 mode is unobservable in the recorded signals, we predict the tuning curves[52] of both modes in Figure 8(b) by using the material properties in Table 1 (only taking the elastic terms), from which the A0 mode's amplitude greatly smaller than the one of the S0 mode is exposed to view. Thus, in the subsequent signal processing, we only focus on the S0 mode.

Dispersion curve identification for energy velocity and attenuation coefficient

Energy velocity and attenuation coefficient identification at 100 kHz. The LR method introduced previously is used to identify energy velocity at a given frequency of 100 kHz in the unmounted FCS experiments, as illustrated in Figure 9(a). The regressed lines for the three groups are plotted based on the scatter points representing the time of arrival (ToA) of the S0 mode's wave packet versus sensing distance, from which energy velocity is identified from the inverse of the slope of the regressed line. The regression results are listed in Table 2, which shows the consistent energy velocities identified amongst the three sensor groups and meanwhile the higher correlation coefficients R^2 (0.99).

Attenuation coefficient can also be identified by using the LR method based on equation (27), as illustrated in Figure 9(b), in which some points of Group 1 are overlapped by the points of Group 2 and 3 because the sensors in Groups 2 and 3 are contained in Group 1. The results extracted from Figure 9(b) are listed in Table 3, from which the R^2 in Group 1 (0.39) is greatly lower than the one of Group 2 (0.92) and

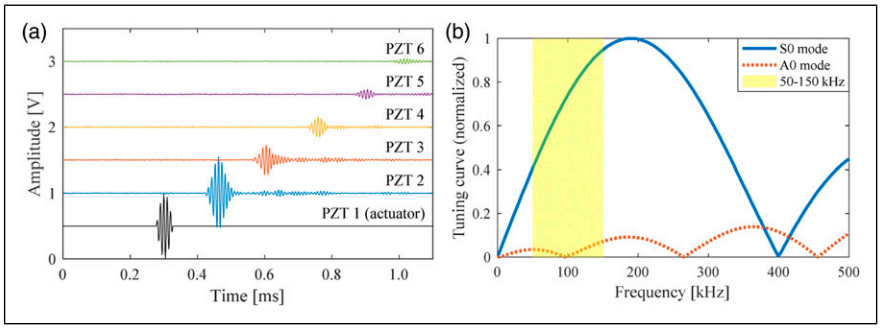

Figure 8. (a) Typical guided wave signals of the unmounted FCS at 100 kHz; (b) Predicted tuning curves of the unmounted FCS. FCS: fan cowl structure.

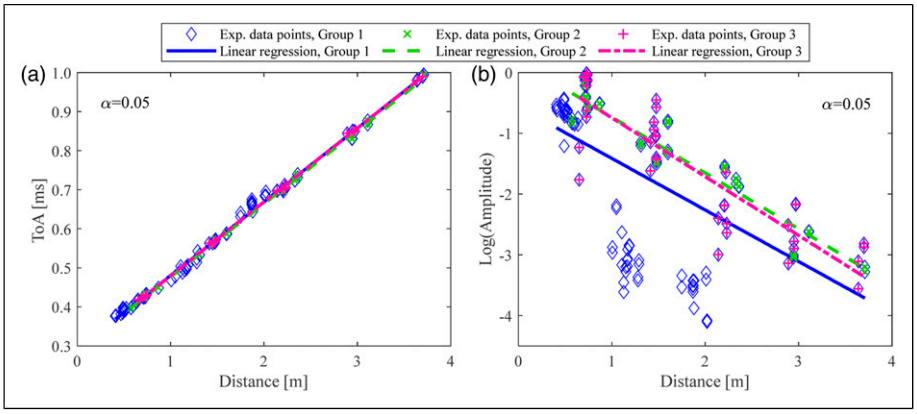

Figure 9. Example of identifying (a) energy velocity and (b) attenuation coefficient via linear regression method at 100 kHz for the unmounted fan cowl structure. Both figures share the same legend and α is used to give the confidence level with $100(1-\alpha)\%$.

Table 2. Identified energy velocities from Figure 9(a). R^2 is the correlation coefficient.

Group 1			Group 2			Group 3		
c_e (m/s)	c_e bound (m/s)	R^2	c_e (m/s)	c_e bound (m/s)	R^2	c_e (m/s)	c_e bound (m/s)	R^2
5308	(5258,5359)	0.99	5340	(5279,5402)	0.99	5291	(5257,5325)	0.99

Group 3 (0.79). This result is consistent with the dispersed scatter points of Group 1 in Figure 9(b). More fundamentally, the lower R^2 in Group 1 is caused by the anisotropic effect of composite materials since the sensors in Group 1 yield multiple directions of propagation paths, whereas Groups 2 and 3 only orient at the horizontal direction; thus, a larger R^2 value is guaranteed respectively for the two groups.

To further illustrate the anisotropic effect of energy velocity and attenuation coefficient, their polar plots of the S0 mode are generated in Figures 10(a) and (b) based on the viscoelastic material properties of HR and KV models listed in Table 1. In both figures, the experimentally identified values of the three groups are depicted as well for comparison, but the data point of Group 1 along 0° direction only plays the reference role given that the propagation paths in Group 1 are actually multi-directional. Observing Figure 10(a), at 0° direction, the model predicted energy velocity is comparable to the experimentally identified ones. In Figure 10(b), the HR model predicts a more accurate value of attenuation coefficient than the KV model. One interesting point from both figures is that unlike the quasi-isotropic property of energy velocity, wave attenuation is heavily influenced by the anisotropic effect of composite materials, which shows that the 0° and 90° directions present the largest and smallest value of attenuation coefficient, respectively. The anisotropic phenomenon of wave attenuation physically explains the dispersed experimental data points in Group 1 of Figure 9(b). In view of the inapplicable LR method to Group 1, only Groups 2 and 3 of the unmounted FCS are employed to identify the attenuation coefficient dispersion curves in the next subsection (see Figure 12(b)).

For the mounted FCS, there is only one frequency testing data, 100 kHz, available. The identified values of the six regions are displayed in Figure 11 in the form of a bar chart, in which the horizontal lines represent the reference values that are obtained from the unmounted FCS counterpart, that is, for energy velocity 5340 m/s and for attenuation coefficient 0.92 Np/m as listed in Group 2 of Table 2 and Table 3, respectively. The red triangular arrows in Figure 11 denote that the marked bars correspond to a R^2 larger than 0.7 which suggests a strong linear correlation. From Figure 11, these findings can be obtained: (1) all the R^2 values of energy velocity in the six regions are larger than 0.7 whereas only nine out of 15 for attenuation coefficient; (2) energy velocities tend to be consistent but the distribution of attenuation coefficients are more variable; and (3) the identified energy velocities in different groups of the six regions agree well with the reference value. However, there exists more discrepancy between the identified attenuation coefficients and the reference one but the same order of magnitude remained. The quality of energy velocity identification is much better than the quality of the attenuation coefficient which may be interpreted as the attenuation coefficient being much smaller than the propagating wavenumber ($|k_i| \ll |k_r|$) and thus much more sensitive to experimental noise. Note that in Figure 11 several bars are not shown because of their unphysical meanings such as too large or too small energy velocity or negative attenuation coefficient, which may be attributed to the superposed S0

Table 3. Identified attenuation coefficient from Figure 9(b). R^2 is the correlation coefficient.

Group 1			Group 2			Group 3		
k_i (Np/m)	k_i bound (Np/m)	R^2	k_i (Np/m)	k_i bound (Np/m)	R^2	k_i (Np/m)	k_i bound (Np/m)	R^2
0.85	(0.66,1.04)	0.39	0.92	(0.81,1.03)	0.92	0.97	(0.80,1.13)	0.79

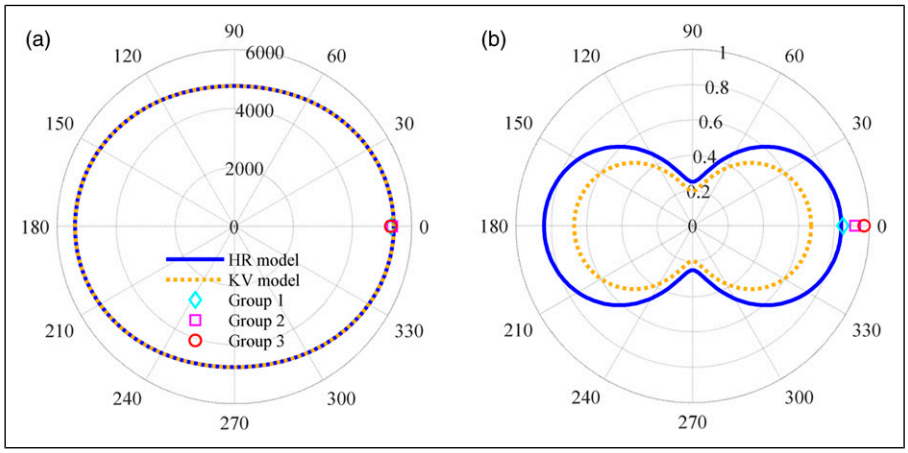

Figure 10. Polar plot of S0 mode of (a) energy velocity [m/s] and (b) attenuation coefficient [Np/m] at 100 kHz for the unmounted fan cowl structure. Both sub-figures share the same legend.

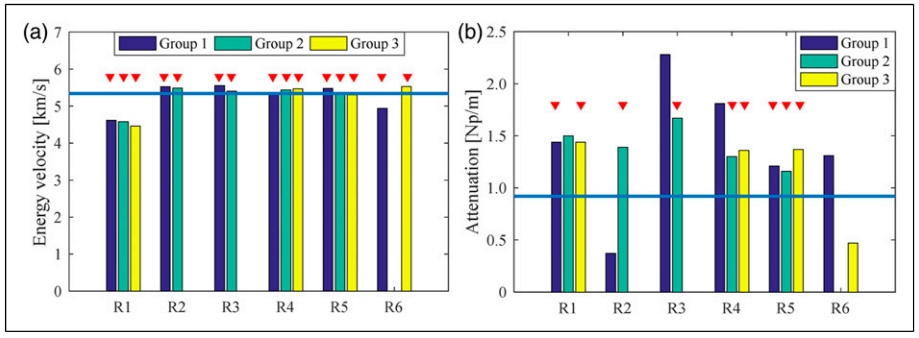

Figure 11. Bar chart to display regression results of (a) energy velocity and (b) attenuation coefficient via linear regression method for the mounted FCS at 100 kHz. The horizontal line represents the reference value of the unmounted FCS, and the red triangular arrows denote that the marked bars correspond to a R^2 larger than 0.7. FCS: fan cowl structure.

mode's wave packet by other modes, for example, A0 or the reflected modes.

Identified dispersion curves of energy velocity and attenuation coefficient. By applying the LR method to each frequency for the unmounted FCS, the dispersion curves of energy velocity and attenuation coefficient are formed in Figures 12(a) and (b), respectively. Note that in Figure 12(a) only the identified curve of Group 1 is presented due to the closing curves amongst the three groups, whereas in Figure 12(b) only the identified curves of Groups 2 and 3 are shown thanks to the anisotropic effect in Group 1 which has been declared in the previous subsection. Additionally, the curves of correlation coefficients R^2 corresponding to Figures 12(a) and (b) are presented in Figure 12(c) to assess the quality of the identified dispersion curves. Obviously, the identified S0 mode's energy velocity curve is accurate because of its greater correlation coefficients (all larger than 0.95). Although the identified attenuation curves (Figure 12(b)) are not as good as the energy velocity curve (Figure 12(a)), we can still get some meaningful findings: (1) in the frequency range 75–150 kHz, the identified attenuation coefficients are reliable enough given that the corresponding R^2 values are larger than 0.7 except the initial

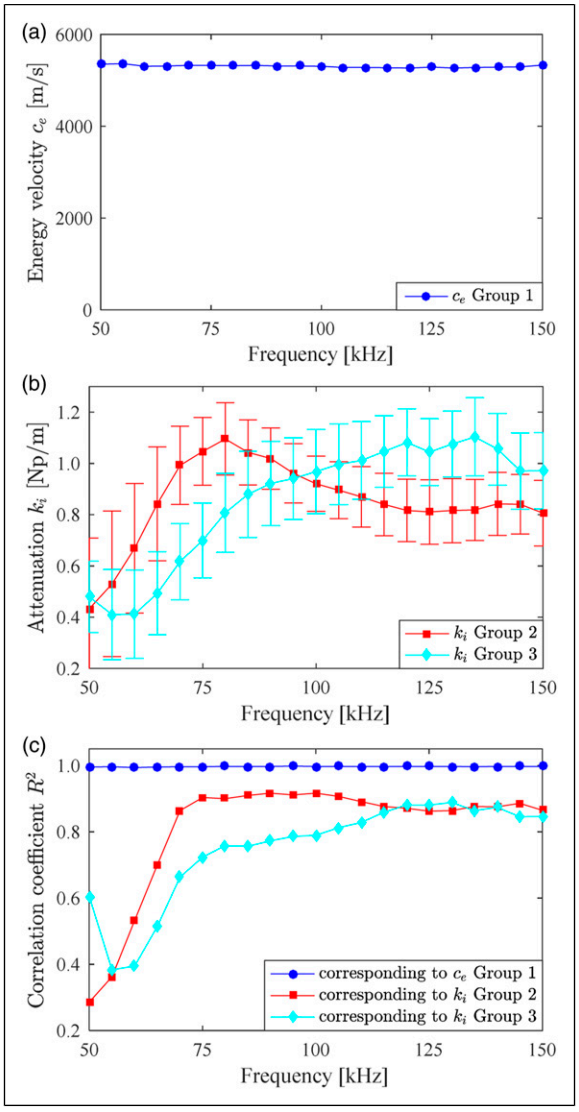

Figure 12. The identified dispersion curves of (a) energy velocity, (b) attenuation coefficient, and (c) correlation coefficient. These sub-figures relate to the S0 mode propagating at 0° direction of the unmounted fan cowl structure.

points (50–70 kHz); (2) both curves present the same trend, that is, attenuation increases with frequency firstly and then decreases; and (3) the identified attenuation coefficients for both groups are equal at approximately 95 kHz, and the lower and upper bounds of the two groups are intersected in the vicinity of 95 kHz.

Estimation of viscoelastic material properties of the unmounted fan cowl structure

The experimentally identified S0 mode attenuation coefficients in Figure 12(b) are further employed to estimate viscoelastic material properties via the least square method formulized in equation (29). When specifying damping models, only HR and KV models are used considering that the BT model is mainly used for highly damped structures whereas FCS is slightly damped because attenuation coefficient is no more than 2 Np/m in the interested frequency range according to Figure 12(b). The estimated viscoelastic properties of the two models are listed in Table 1. From this table, for both models, γ_1 is greatly larger than the remaining five parameters, meaning that the damping effect is predominated in the principal fiber direction of composite lamina. Besides, the loss factors of the KV model are the relative values to the ones at the characterization frequency f_c =250 kHz. If f_c changes to a different value, the loss factors of the KV model will change correspondingly (but the ratio $\boldsymbol{\gamma}_{KV}/f_c$ keeps unchanged).[40]

Once all the required material parameters in Table 1 have been obtained, they are used as inputs to the developed algorithm exhibited in Figure 4. After computing, the dispersion curves of energy velocity and attenuation coefficient for the two damping models are depicted in Figures 13(a) and (b), respectively, in which the experimentally identified data points in Figures 12(a) and (b) are also presented for comparison. Figure 13(a) shows that the computed S0 mode energy velocity curve agrees well with the experimental points, among which the diamond point is the mean value of the bars in Figure 11(a), representing the mounted FCS. Besides, the two damping models produce the mutually overlapped energy velocity curves for the three basic modes in the shown frequency range, denoting that the viscoelastic damping effect does not change the property of energy velocity for the slightly damped FCS.

Figure 13(b) shows that the curve of the HR model presents the linear trend whereas the curve of the KV model expresses the parabola trend, which results in overestimated attenuation prediction in higher frequency range. Furthermore, the upward concavity of the curve of the KV model is contrary to the upward convexity of the experimental data points; thus, the HR model fits better with the experimental data than the KV model, and thanks to this reason, the HR model will be adopted to predict attenuation coefficient in the next subsection. Note that the diamond point in Figure 13(b) is the mean value of the marked bars in Figure 11(b), representing the mounted FCS, and its lower and upper bounds are the minimum and maximum values of the marked bars in Figure 11(b).

Attenuation coefficient prediction for the unmounted fan cowl structure

By using the elastic and viscoelastic parameters of the HR model in Table 1, the attenuation coefficient can be predicted in two ways. One is the traditional dispersion curve in a wide frequency range at a fixed propagation direction $\theta = 180^\circ$ as depicted in Figure 14(b), and another one is

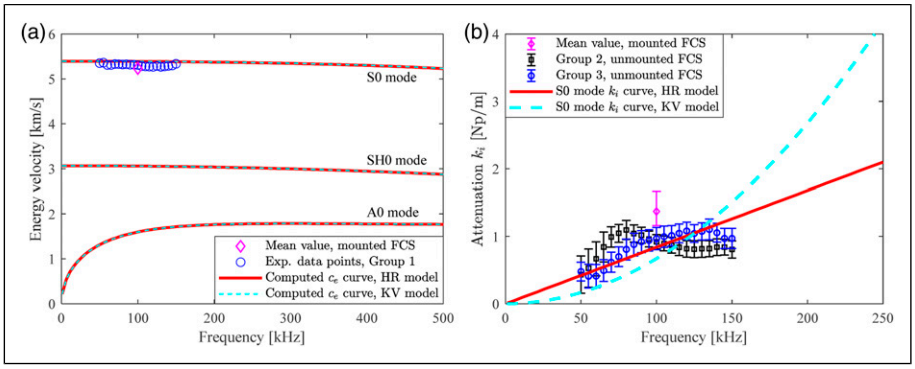

Figure 13. Comparison between the computed and experimentally identified dispersion curves of (a) energy velocity and (b) attenuation coefficient for the unmounted fan cowl structure at $\theta = 0^{\circ}$.

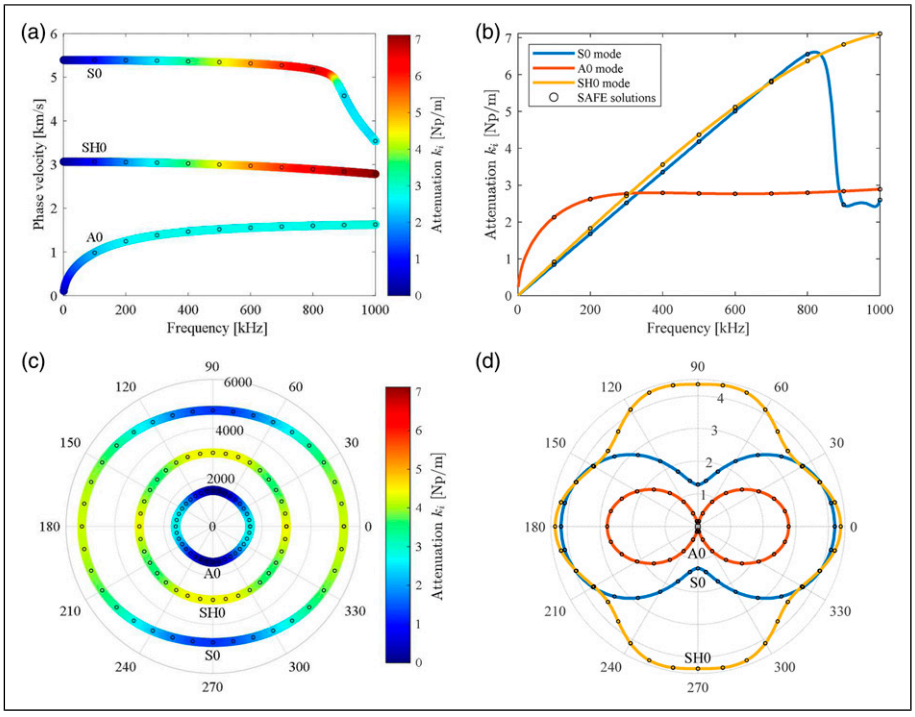

Figure 14. For the unmounted fan cowl structure, Hysteretic model's prediction of (a) dispersion curve of phase velocity at $\theta = 180^{\circ}$, (b) dispersion curve of attenuation coefficient at $\theta = 180^{\circ}$, (c) polar plot of phase velocity [m/s] at f =500 kHz, and (d) polar plot of attenuation coefficient [Np/m] at f = 500 kHz. The open circles in the four sub-figures are the solutions computed by the semi-analytical finite element method.

the polar plot representing the distribution of attenuation coefficient for all propagation directions at a fixed frequency f =500 kHz as illustrated in Figure 14(d). Besides, the two displaying ways are also applied to phase velocity in Figures 14(a) and (c), in which the color code on the curves is the attenuation coefficient superimposed from Figures 14(b) and (d). With the colored diagrams, the dispersion property of phase velocity and attenuation can be explored in the same Figure 14(a), and the anisotropic degree of both quantities can be simultaneously compared in Figure 14(c).

Comparing Figure 14(a) and (b), phase velocity presents slight dispersion property in most of the frequency range, whereas attenuation coefficient increases in the same frequency range except for the S0 mode after 820 kHz, which shows a sudden drop (see Figure 14(a) and (b)). Besides, A0 mode attenuation is larger than the one of the S0 mode in the tested frequency range of 50–150 kHz. This again explains why only the S0 mode wave packet is discernible in the recorded wave signals (see Figure 8(a)) since the A0 mode wave packet has been rapidly attenuated. Comparing Figure 14(c) and (d), phase velocities of the three basic

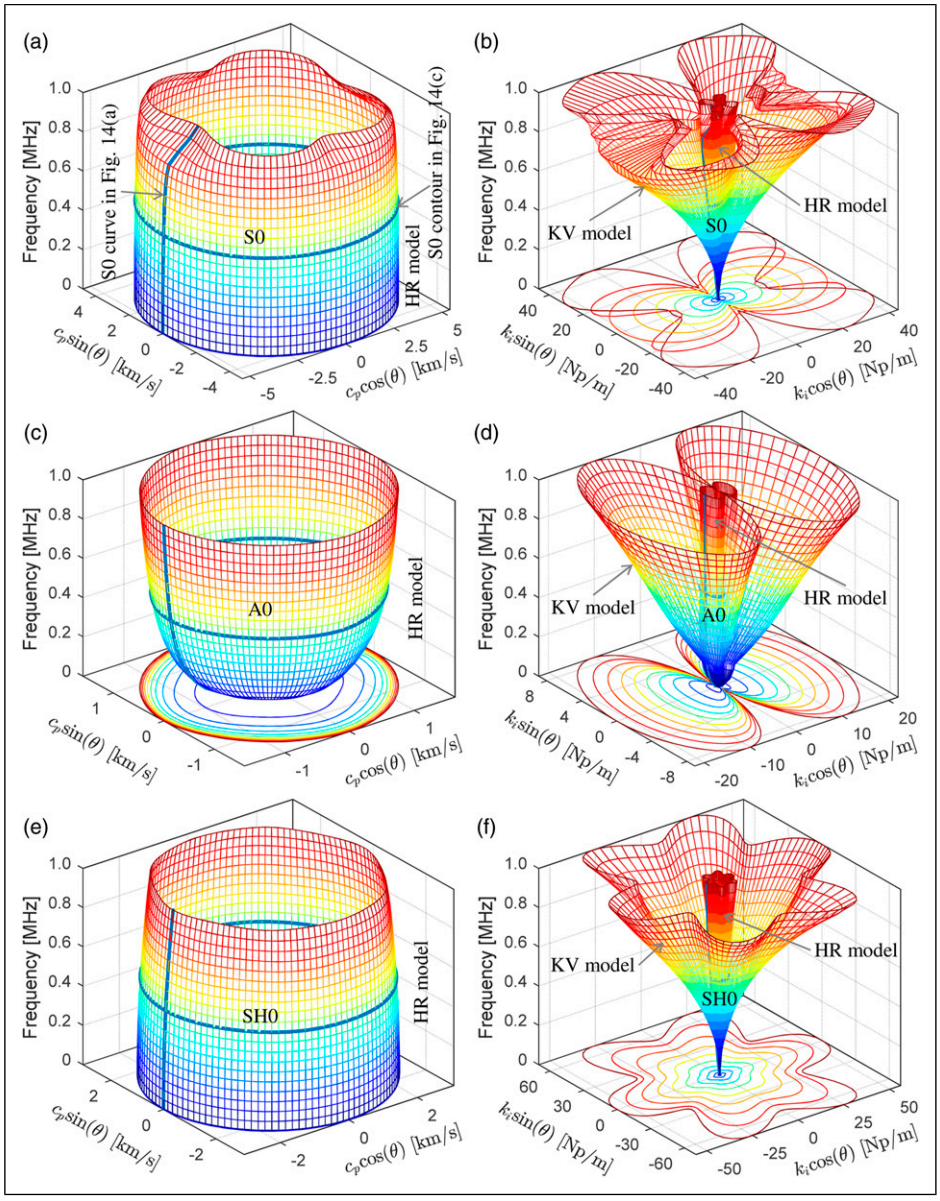

Figure 15. For the unmounted fan cowl structure, surface plot of phase velocity (left) and attenuation coefficient (right): (a) and (b) S0 mode, (c) and (d) A0 mode, (e) and (f) SH0 mode. The inner and outer surfaces in sub-figures (b), (d), and (f) correspond to Hysteretic and Kelvin–Voigt models, respectively.

modes present a consistent quasi-isotropic behavior, whereas attenuation coefficients are anisotropic for the three considered modes. Figure 14(d) clearly shows that S0 and A0 modes possess larger and smaller attenuation in the principal (0° and 180°) and minor (90° and 270°) directions, respectively. Attenuation of the SH0 mode is less variable, the smallest value appearing at 30° in the first quadrant. Note that the open circles in Figure 14 are the solutions of SAFE method[32,34] that is used here for comparison and verification with the proposed dGMM approach. For SAFE computation in this instance, five 1D quadratic elements per layer are used to mesh the through thickness section of the four-layered [0/−45/+45/0] composite laminate, which guarantees its convergence as proved in Figure 14.

The 3D surface diagrams for the three basic modes are shown in Figure 15 to unveil the relation between frequency, propagation angle, and phase velocity or attenuation coefficient. In another sense, the frequency-spatial spectrum of the two quantities is plotted here. The surface plots can be generated in two ways that are derived from Figure 14. Consider the example in Figure 15(a): one way is to "*spin*" the phase velocity curve of the S0 mode in Figure 14(a) with propagation angle, and another one is to "*extrude*" the phase velocity contour of the S0 mode in

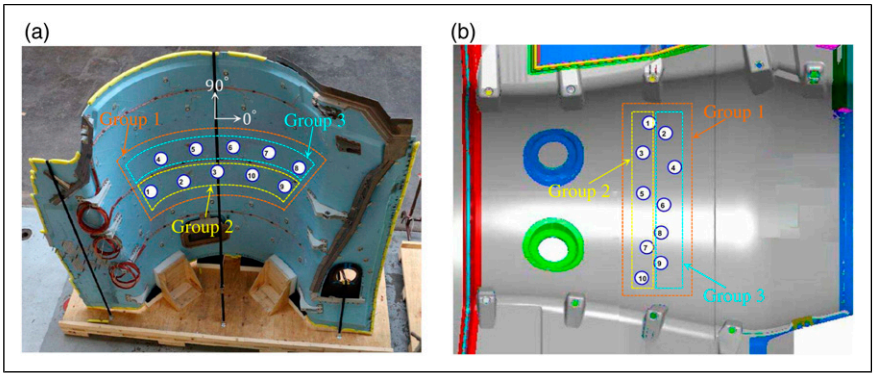

Figure 16. The transducers layout of the inner fixed structure for (a) the unmounted case and (b) the mounted case on an instrumented A380 plane.

Table 4. Elastic material properties of the carbon epoxy ply in the unmounted inner fixed structure.

(E_1,E_2,E_3) (GPa)	(G_{23},G_{31},G_{12}) (GPa)	$(\nu_{12},\nu_{13},\nu_{23})$	ρ (kg/m^3)	Ply thickness (mm)
(51.0,65.7,8.1)[a] (40.0,55.0,8.1)[b]	(5.2,5.2,5.2)	(0.02,0.3,0.3)	1554	0.28

[a] The original values from Ref. 39 that lead to a great agreement to the experimental data of the unmounted IFS.
[b] The updated values that result in the best match with the experimental data of the mounted IFS.

Table 5. Elastic material properties of the aluminum core layer in the unmounted inner fixed structure.

E (MPa)	G (MPa)	ν	ρ (kg/m^3)	Layer thickness (mm)
866	354	0.2232	67	1.2

Figure 14(c) along the frequency axis. Due to the quasi-isotropic property of phase velocity, its surface plot presents a cylindrical shape for each considered mode, whereas the shape of the attenuation coefficient is multifarious for different modes. This phenomenon reveals again that in the frequency-spatial spectrum, attenuation coefficient behaves in an anisotropic manner even if the current composite laminate of FCS is quasi-isotropic from the phase velocity point of view. As a consequence, obtaining a precise characterization of attenuation is in practice more complex than for phase velocity. Note that in Figures 15(a), (c) and (e), only HR model's predictions are presented since the KV model produces very similar diagrams. In Figures 15(b), (d), and (f), both HR and KV models' diagrams are depicted with the inner and outer surfaces belonging to HR and KV models, respectively.

Case study on an unmounted and mounted inner fixed structure of A380 plane

Experimental setup

To further demonstrate the effectiveness of the proposed wave attenuation prediction method, two cases of IFS either unmounted or mounted on an instrumented A380 plane are investigated in this section. The sketch picture of this structure is shown in Figure 1(b), along with its geometrical dimensions given in the introduction section, and its actual profile is presented in Figure 16(a). The IFS is a sandwich-type structure consisting of an aluminum alloy honeycomb core and two four-plies carbon epoxy outer skins with stacking sequence [0/−45/+45/0/Al/0/+45/−45/0]. The total thickness of the sandwich plate is 3.44 mm. The elastic material properties of the composing laminae can be obtained from Fendzi's PhD thesis[39] and are listed in Tables 4 and 5 for convenience. Table 6 lists the viscoelastic properties of the two materials corresponding to the specific damping models, which are obtained through the model updating process (see the subsection Estimation of Viscoelastic Material Properties of the Unmounted IFS) since the viscoelastic information is not available from this reference.

There are in total 10 PZTs surfaces installed on the unmounted and mounted IFS, which are arranged into three groups for each case as illustrated in Figure 16. The orientation of the 0° layer of carbon epoxy lamina in the plate is unknown but assumed to be along the alignment direction of the sensors in Group 2 or 3 of Figure 16(a) considering that this direction can result in the best match between the theoretical predictions and experimental measurements for both energy velocity and attenuation coefficient. The signal acquisition process was similar to the experiments on FCS and thus the detailed experimental setup is not shown for brevity. The frequency series in the unmounted IFS experiment were swept from 50 kHz to 150 kHz at 5 kHz increment but there

Table 6. Viscoelastic material properties of the carbon epoxy ply and aluminum core in the unmounted inner fixed structure.

Combination of damping models	Carbon epoxy ply (HR or KV)							Aluminum core (BT)		
	γ_1	γ_2	γ_3	γ_{23}	γ_{31}	γ_{12}	f_c (kHz)	γ_E	γ_G	ϵ
HR + BT model[a]	13.9%	0.04%	0.02%	5.60%	5.60%	5.60%	—	19.9%	19.9%	10
KV + BT model[b]	27.4%	0.01%	0.01%	0.01%	0.01%	0.01%	250	30.0%	30.0%	10

[a] The HR model is used for carbon epoxy plies and the BT model is applied for aluminum core.
[b] The KV model is used for carbon epoxy plies and the BT model is applied for aluminum core.

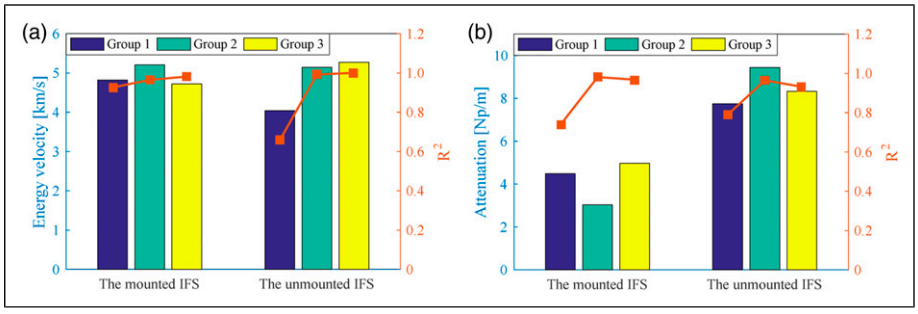

Figure 17. Comparison between the mounted and unmounted inner fixed structure for (a) energy velocity and (b) attenuation coefficient at 100 kHz. In the two sub-figures, the bars relate to the left y-axis and the lines correlate to the right y-axis.

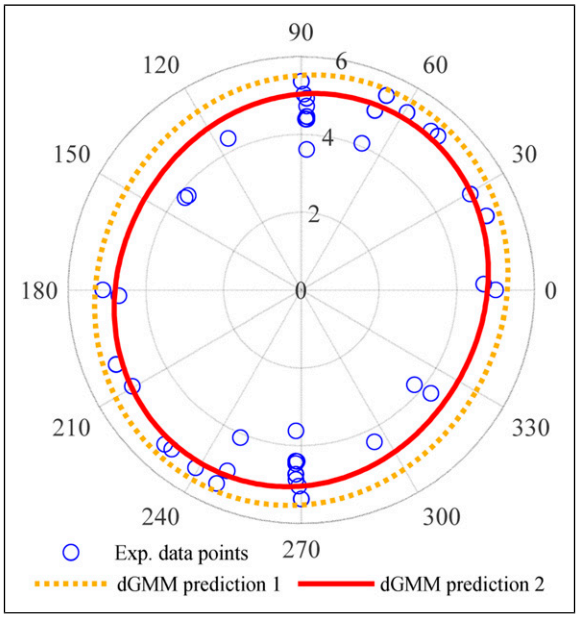

Figure 18. Polar plot of S0 mode energy velocity [km/s] in the mounted inner fixed structure at 100 kHz. The contour of dGMM prediction 1 and dGMM prediction 2 are computed by using the (E_1,E_2,E_3) values a and b in Table 4, respectively. dGMM: damped global matrix method.

was only 100 kHz available for the mounted IFS experiment. Time averaging and wavelet denoising strategies were also adopted for signal processing.

Dispersion curve identification for energy velocity and attenuation coefficient

Comparison of energy velocity and attenuation coefficient at 100 kHz between the mounted and unmounted inner fixed structure. Figure 17(a) presents the comparison of the identified energy velocity via the LR method between the mounted and unmounted IFS at 100 kHz as this frequency is unique for the mounted case. This sub-figure shows that both cases produce close energy velocities and simultaneously the higher R^2 values larger than 0.8 are obtained except the Group 1 of the unmounted IFS. Thus, Groups 2 and 3 of the unmounted IFS will be adopted to identify the dispersion curves of energy velocity in the next subsection.

A similar comparison of the identified attenuation coefficient is illustrated in Figure 17(b). It shows that overall, the mounted IFS returns about half the attenuation of its unmounted counterpart. This could be attributed to different environmental conditions in both cases, and especially to the fact that when IFS is mounted on an A380 plane, the structure is stressed which can influence guided waves propagation properties.[53] Moreover, the attenuation coefficient of Group 2 is not equal to the one of Group 3 for both cases and the discrepancy in the mounted IFS is more salient, even though Group 2 and 3 have the same propagation direction. This phenomenon can be explained by the fact that the imaginary part of the wavenumber, that is, the attenuation coefficient, is much smaller than the real part

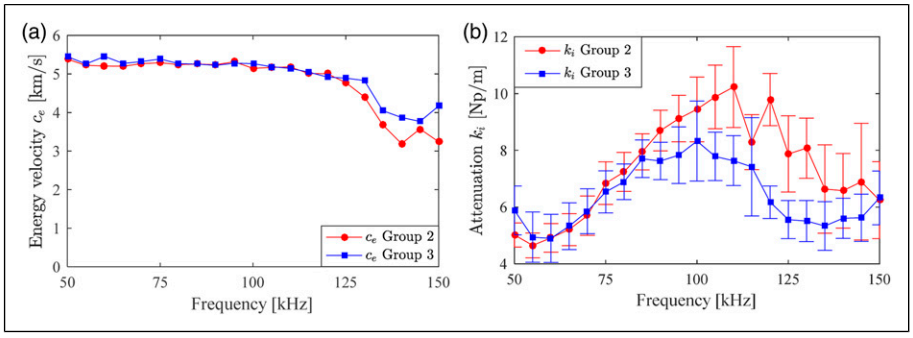

Figure 19. The identified S0 mode dispersion curves of (a) energy velocity and (b) attenuation coefficient for the unmounted inner fixed structure.

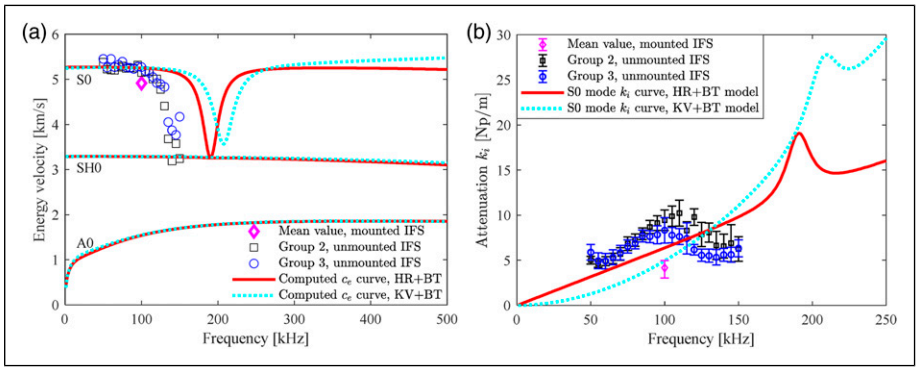

Figure 20. Comparison between the computed and experimentally identified dispersion curves of (a) energy velocity and (b) attenuation coefficient for the unmounted inner fixed structure at $\theta = 0^{\circ}$.

and thus much more prone to noise error. Since the correlation coefficients of Groups 2 and 3 of the unmounted IFS are larger than 0.8, the two groups will be selected to identify dispersion curves of attenuation coefficient in the next subsection.

To further explore directional dependence of the S0 mode energy velocity, the guided wave signals in Group 1 of the mounted IFS were processed to generate a polar plot of energy velocity, as depicted in Figure 18, since this group possesses multiple wave propagation directions. Besides, the theoretical curves predicted via the developed dGMM method are also presented in Figure 18 for comparison purpose. The curves of dGMM prediction 1 and dGMM prediction 2 are created by using the (E_1,E_2,E_3) values a and b listed in Table 4, respectively. The other material properties listed in Table 4 and Table 5 are the same. Figure 18 shows that the original (E_1,E_2,E_3) values a yield to an overestimated prediction (the curve of dGMM prediction 1). When these values are updated to values b, the predicted curve of dGMM prediction 2 matches well with the experimental data points of the mounted IFS, which is the same structure as the unmounted counterpart but undergoing different environmental conditions, that is, existing stress in the mounted case thus modifying wave propagation properties.[53] Figure 18 shows that the IFS structure holds quasi-isotropic property in terms of S0 mode energy velocity that is consistent with the symmetric stacking sequence of laminae [0/−45/+45/0/Al/0/+45/−45/0].

Identified dispersion curves of energy velocity and attenuation coefficient. The identified dispersion curves of energy velocity and attenuation coefficient of the unmounted IFS are generated in Figure 19(a) and (b), respectively. Note that the corresponding correlation coefficient curves are not presented here because all values are larger than 0.8 which demonstrates reliable results of dispersion curves identification. Observing Figure 19(a), the energy velocity curves of both groups basically overlap to each other, whereas in Figure 19(b), Group 3 brings a lower attenuation than Group 2, but both curves keep the same tendency as the unmounted FCS, as seen in Figure 12(b). Figure 19(b) reveals that for practical aeronautic composite structures, the attenuation mechanism induced by material damping is more complex than for a unidirectional CFRP composite plate.[34] The lower and upper bounds in Figure 19(b) represent the confidence intervals which are extracted from the LR method under 95% confidence level.

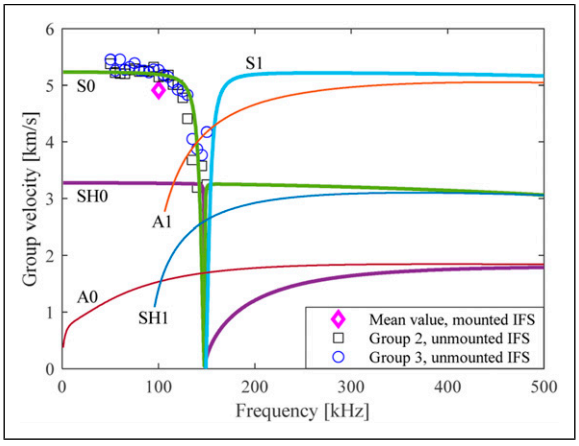

Figure 21. The computed group velocity via the pure elastic global matrix method for the unmounted inner fixed structure at $\theta = 0^{\circ}$.

Estimation of viscoelastic material properties of the unmounted inner fixed structure

With the experimentally identified attenuation coefficients in Figure 19(b), the viscoelastic material properties of the unmounted IFS can be estimated according to the model updating process formalized in equation (29). Before performing this process, one has to note that the attenuation of the unmounted IFS is larger than the one of FCS according to Figure 19(b), thus the BT model should be applied to IFS in a certain form considering that the BT model is mainly used for highly damped structures,[41] and the unmounted IFS exactly belongs to this case. Furthermore, the IFS is a sandwich-type structure composed of two inhomogeneous materials with the aluminum alloy honeycomb core and the carbon epoxy skin layers. Therefore, the core layer and the skin layers can be modeled by different damping models. By following the convention in FCS, the carbon epoxy layers in IFS are modeled by HR or KV models, thus the BT model is naturally applied to the aluminum alloy core layer, which finally results in two combinations of damping models, HR+BT and KV+BT models.

By taking the identified attenuation coefficients in Figure 19(b) as the training data to the model updating process, the estimated viscoelastic material properties of the two combinations of damping models are obtained in Table 6. It shows that the parameters of the BT model in the aluminum alloy core layer are larger than the parameters of the HR or KV model in the carbon epoxy layers, thus manifesting that the large attenuation of IFS is controlled by the highly damped aluminum alloy honeycomb core layer.

With the obtained viscoelastic material properties of the two combinations of damping models in Table 6, the energy velocity and attenuation curves are theoretically computed via the developed dGMM as depicted in Figures 20(a) and (b), respectively, in which the experimentally identified data points in Figures 19(a) and (b) are also presented for comparison, along with the diamond points in Figures 20(a) and (b) being the mean values of the mounted IFS in Figure 17(a) and (b), respectively.

We firstly analyze Figure 20(b). It shows that the linear trend curve of the HR+BT model in the frequency range of 0–150 kHz fits better with the experimental data than the parabola trend curve of the KV+BT model in 0–200 kHz. Since the concavity of the KV+BT model's curve is reversed to the trend of the experimental data points, the KV+BT model predicts underestimated and overestimated attenuation in the lower and higher frequency range, respectively. For the HR+BT model, its linearized prediction represents the average effect on the experimental data in the least square sense.

Then, we analyze Figure 20(a). It shows that, for the two combinations of damping models, the computed S0 mode energy velocity curves do not agree well with the experimental data, and the KV+BT model produces more deviations than the HR+BT model in the frequency range of 100–150 kHz. However, when we compute the group velocity via equation (22) by using the pure elastic material properties listed in Table 4 and Table 5, that is, performing the undamped GMM,[42] one interesting phenomenon occurs. The computed S0 mode group velocity curve matches very well with the experimental data as observed in Figure 21. This phenomenon reveals the fact that, for the sandwich-type structure made of inhomogeneous materials, the damping mechanism adopted has a great influence on wave propagation speed. And the model parameters (both the elastic constants and the loss factors) should be updated in order to get a better fit to both experimental energy velocity and attenuation data which could be one of the future works.

Back to Figure 20(a), from the point of computation, HR+BT and KV+BT models produce a mutually overlapped energy velocity curves for SH0 and A0 modes in the shown frequency range, which is different from the discrepant S0 curves computed with the two models.

Prediction of dispersion curves in various forms for the unmounted inner fixed structure

The two combinations of damping models are further employed to predict the dispersion curves in the 3D space (f, k_r, k_i) at the fixed propagation angle $\theta = 90^{\circ}$ as depicted in Figures 22(a) and (b) for HR+BT and KV+BT models, respectively. These modal curves are classified into symmetric and anti-symmetric modes by checking the symmetry conditions of the displacement mode shapes based on equation (20), which are not presented in this

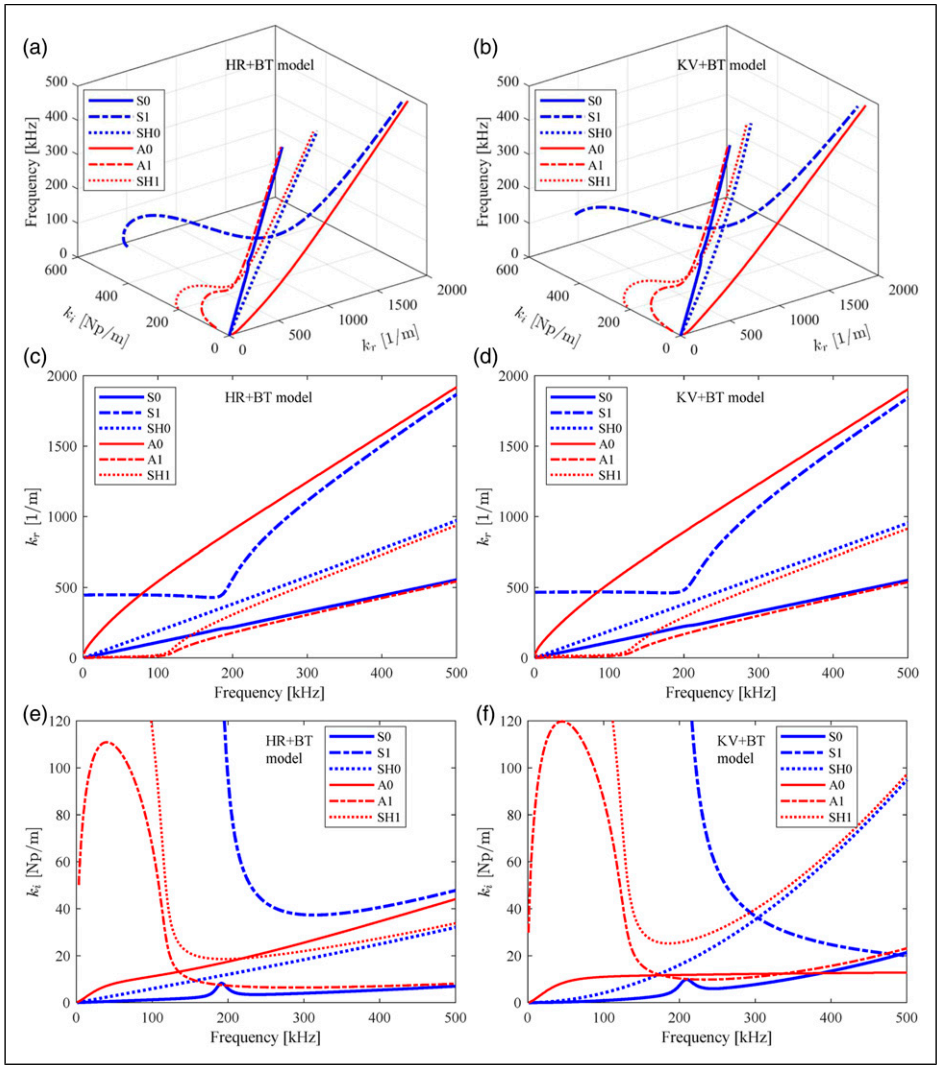

Figure 22. For the unmounted IFS, the predicted dispersion curves at $\theta = 90^{\circ}$ for the HR + BT model (left) and the KV + BT model (right): (a) and (b) 3D space of (f,k_r,k_i), (c) and (d) projection onto (f,k_r) plane, (e) and (f) projection onto (f,k_i) plane.

paper for the sake of brevity. For a certain combination of damping model, the 3D curves in Figures 22(a) and (b) are projected onto the (f,k_r) plane and the (f,k_i) plane to make a comparison of the two combinations of damping models. According to Figures 22(c) and (d), HR+BT and KV+BT models predict identical propagating wavenumbers for the six modes in the shown frequency range, whereas the two combinations of damping models predict different attenuation coefficients, especially for SH0 and A0 modes, according to Figure 22(e) and (f). Thus, choosing the proper damping model (or their combinations) is the key to accurately predict wave attenuation here. Figure 22(c) and (d) also indicate that there is no cutoff frequency for S1, A1, and SH1 modes, which is accompanied by a large attenuation in the lower frequency range as shown in Figure 22(e) and (f). This behavior is a unique property of the damped waveguide.[17]

To study the influence of attenuation on phase velocity, the attenuation curves of S0, A0, and SH0 modes in Figure 22(e) are separately drawn in Figure 23(b), then superimposed on the phase velocity curves in color code as illustrated in Figure 23(a). This sub-figure shows that there is a step in the S0 mode phase velocity curve around 200 kHz, which is caused by the fluctuation of the S0 mode attenuation curve around 200 kHz in Figure 23(b). Besides, the S0 mode holds a slight attenuation in comparison with SH0 and A0 modes. This could be the reason that only S0 mode information has been identified experimentally (see Figure 19) as SH0 and A0 modes have been rapidly attenuated. In short, Figures 23(a) and (b) manifest that the phase velocity of guided waves in a damped sandwich

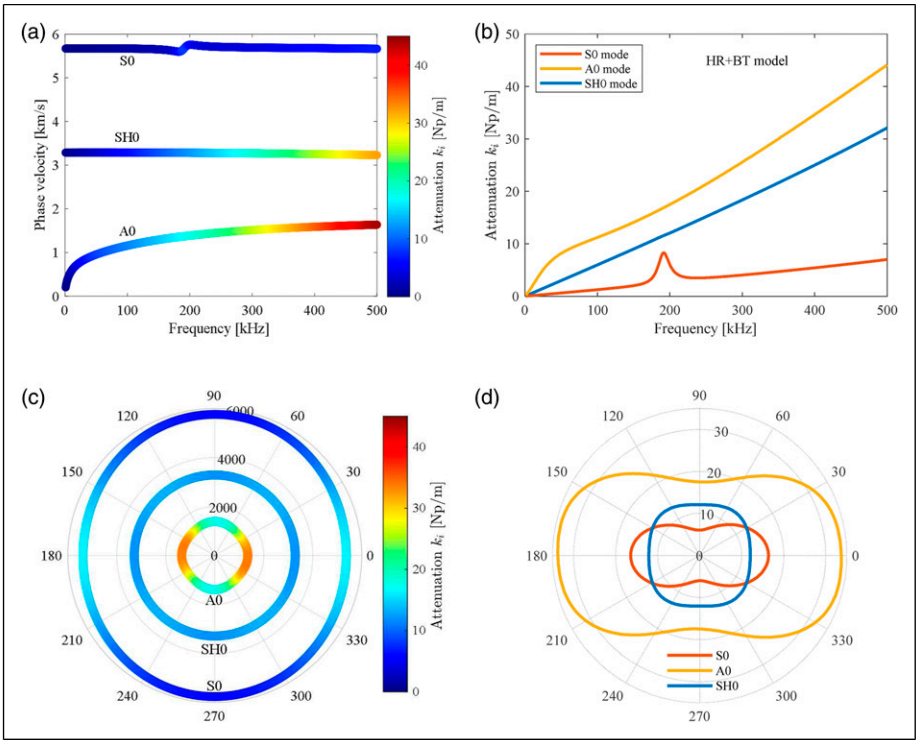

Figure 23. For the unmounted inner fixed structure, HR + BT model's prediction of (a) dispersion curve of phase velocity at $\theta = 90^{\circ}$, (b) dispersion curve of attenuation coefficient at $\theta = 90^{\circ}$, (c) polar plot of phase velocity [m/s] at f =200 kHz, and (d) polar plot of attenuation coefficient [Np/m] at f =200 kHz.

structure is characterized simultaneously by frequency (dispersion property) and attenuation (viscoelastic damping).

To study the anisotropic effect of phase velocity and attenuation, the polar plots of both quantities are depicted in Figures 23(c) and (d) at the same frequency f =200 kHz. Figure 23(c) displays the quasi-isotropic property of phase velocity of the three basic modes. Nevertheless, pure anisotropic behavior of attenuation is observed in Figure 23(d) for S0 and A0 modes, both of which hold the largest and smallest attenuation in the principal (0° and 180°) and minor (90° and 270°) directions, respectively. As for SH0 mode's attenuation, its anisotropic degree is slight along with the omnidirectional propagation angles. In other words, Figures 23(c) and (d) give the evidence that despite the quasi-isotropic property, attenuation of guided waves in damped sandwich structure still possesses an anisotropic effect.

Finally, the 3D surface diagrams of the three basic modes are predicted in Figure 24 to represent the frequency-spatial spectra of phase velocity and attenuation. In Figures 24(a), (c), and (e), the cylindrical surfaces of S0 and SH0 modes and the paraboloid of revolution of A0 mode signify the quasi-isotropic property of phase velocity. However, the manifold shapes of attenuation in Figures 24(b), (d) and (f) again indicate the anisotropic property of attenuation in the frequency-spatial spectrum. Note that in Figures 24(a), (c), and (e), the KV + BT model's predictions are not presented since it yields almost the same diagrams as the HR + BT model. According to Figures 24(b) and (f), the HR+BT model predicts the same shape of attenuation for the S0 and SH0 modes as one of the KV+BT models but with different scale. However, in Figure 24(d), there is much deviation in the shape of the attenuation for the A0 mode between both models at high frequency. This is because A0 mode attenuation is predicted by using the viscoelastic material properties in Table 6 which is based on the rare information of S0 mode attenuation and only along a single direction ($\theta = 0^{\circ}$). Furthermore, IFS is a honeycomb core sandwich structure being inhomogeneous in nature that leads to much uncertainty in modeling.

The traditional curve in Figure 23 can be reconstructed from Figure 24. For instance, the S0 curve in Figure 23(b) is just the intersecting line of the plane $\theta = 90^{\circ}$ (in the cylindrical coordinate system) to the surface of the HR+BT model in Figure 24(b), and the SH0 contour in Figure 23(d) is the intersecting line of the plane f =200 kHz to the surface of HR+BT model in Figure 24(f). For brevity, these intersecting lines are not depicted in Figure 24. Thus, the frequency-spatial spectra of guided waves will convey more information than the traditional dispersion curves, and it

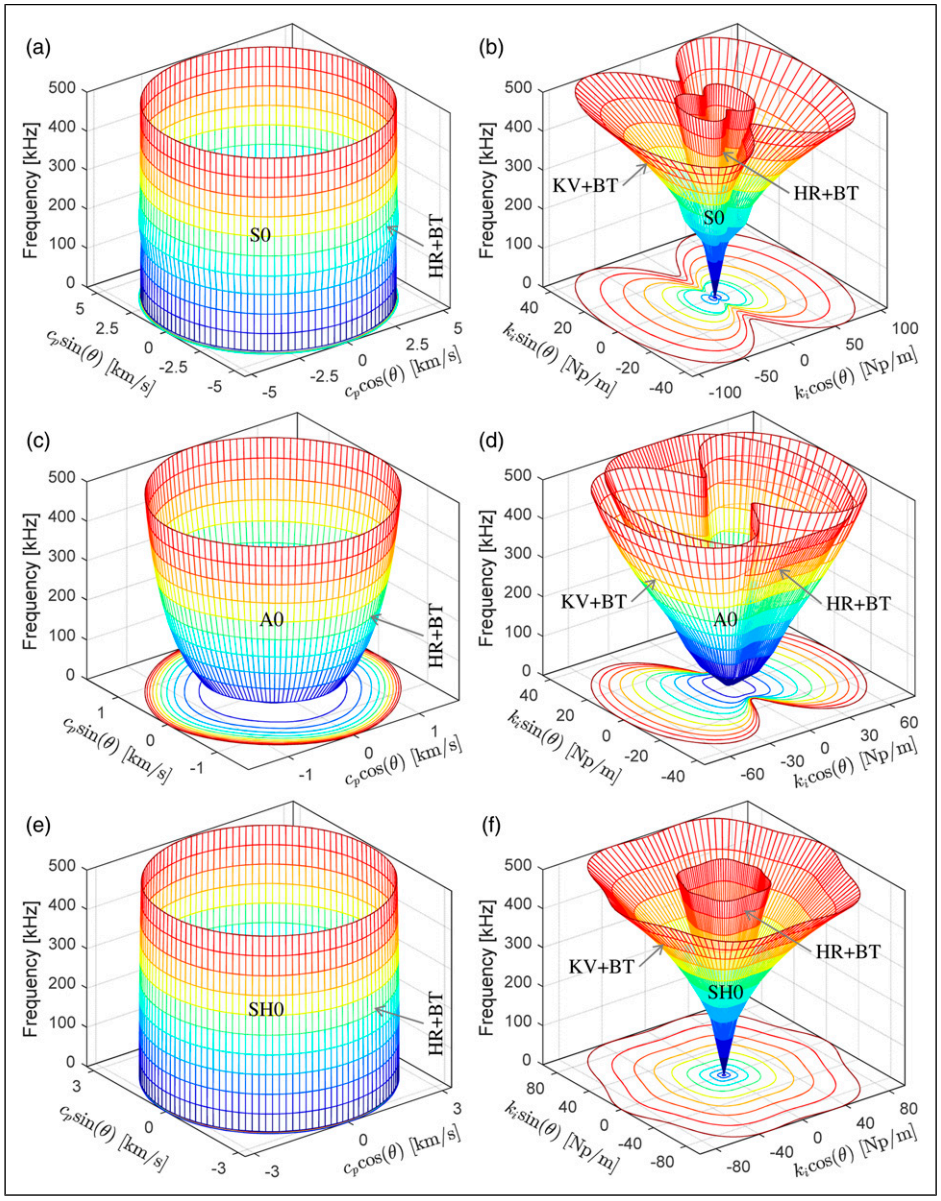

Figure 24. For the unmounted inner fixed structure, surface plot of phase velocity (left) and attenuation coefficient (right): (a) and (b) S0 mode, (c) and (d) A0 mode, (e) and (f) SH0 mode.

will play a more important role in guided wave-based SHM, especially for anisotropic viscoelastic materials.

Discussion and future work

Discussion

Although this paper only presents the comparison results of the S0 mode between the experimental and predicted data, the developed dGMM method can be generalized to other guided wave modes such as A0 and SH0 modes if these modes' information is experimentally identifiable such that the identified data can be integrated to update the viscoelastic material properties. However, simultaneously identifying S0 and A0 modes usually requires special setup of transducers from the hardware viewpoint that have flexible polarity directions, dual PZT for example,[37] to sufficiently excite both fundamental modes. Besides, from the software viewpoint, any efficient decomposition algorithms are required that can separate coupled S0 and A0 wave packets in the signal processing level.[16] To acquire the SH0 wave signal, special SH wave transducers need to be utilized.[54]

This paper takes the damping effect of the elastic moduli into consideration. In some references,[34,55] the

complex stiffness tensor is employed, that is, $C^{*}_{ij}(\omega) = C^{'}_{ij}(\omega) - \mathrm{i}C^{''}_{ij}(\omega)$, to represent the viscoelasticity of composite materials by specifying a certain damping model for the imaginary part $C^{''}_{ij}(\omega)$. However, this utilization increases the number of variables for the model updating process, thus demanding advanced optimization algorithms.[56]

In literature, the KV model is increasingly adopted to compute the 3D dispersion curves in (f,k_r,k_i) domain no matter which numerical method is used.[23,34] In contrast with this tendency, the two case studies in this paper demonstrate that the HR involved models predict more accurate attenuation than the KV involved models in comparison with the experimental data. This fact reveals that choosing a damping model to represent the viscoelasticity of composite materials is application dependent.

Future works

Due to the existence of uncertainties, the predicted energy velocity and attenuation coefficient do not always match well simultaneously with the respective experimental data (see Figure 20). In this situation, the model updating process should yet involve in the identified energy velocity and the elastic constants. That finally leads to the multiple objective optimization problem as presented in equation (30), which is the first work to be studied in the future

$$\widehat{\boldsymbol{\gamma}} = \underset{\boldsymbol{\gamma},E_i,G_{ij},\nu_{ij}}{\arg\min} \left\{ \begin{array}{l} \sum_{l=1}^{m} \left[\mathcal{K}(\boldsymbol{\gamma},\omega_l) - \tilde{k}_{i,l} \right]^2 \\ \sum_{l=1}^{m} \left[\mathcal{C}_e(\boldsymbol{\gamma},\omega_l) - \tilde{c}_{e,l} \right]^2 \end{array} \right\} \tag{30}$$

The second one is to integrate the predicted attenuation into the optimal sensor network deployment procedures. Indeed, when designing a sensor network, one faces two practical issues: the first one is to get sure that all the structures under study will be covered by guided waves and thus that any potential damage position can be inspected; the second one is to get sure that guided waves with enough amplitude will be reflected from the damage toward piezoelectric elements. To solve these issues, precise prediction of the spatial distribution of attenuation is of great concern.

The third work is to improve the traditional damage localization methods such as delay-and-sum,[57] RAPID[9], and Excitelet[58] by taking the viscoelasticity into consideration. Among these methods, temporal or frequency information is usually employed, for example, ToA for delay-and-sum, and wavenumber analysis for Excitelet. In the anisotropic viscoelastic plates, attenuation can change some properties of the temporal and frequency information. Thus, improvement can be made by bridging the gap between attenuation and the temporal- or frequency-based damage localization methods.

Last but not least, exactly predicting the guided wave attenuation for complex structures is always of prime importance, and thus, more profound damping models should be adopted, for example, the rational model[59] described in equation (31). But there are two main fatal issues before implementing this model. (1) There is not a unique principle to determine the number of parameters n appearing in the numerator and denominator of equation (31). (2) Even if n is known, it is still difficult to estimate the coefficients α_i and β_i from experimental attenuation data through the model updating process given that there are six complex moduli $E^{*}_1(\omega)$, $E^{*}_2(\omega)$, $E^{*}_3(\omega)$, $G^{*}_{23}(\omega)$, $G^{*}_{31}(\omega)$, $G^{*}_{12}(\omega)$ in equation (4) and for each modulus, there are $2n$ parameters in equation (31), thus the total number of variables to be determined is large to $12n$ for a single viscoelastic material, which poses a formidable challenge to the model updating process. To implement this damping model for attenuation prediction, more information should be provided firstly

$$E^{*}(\omega) = E_0 \left[\frac{1 + \sum_{i=1}^{n} \beta_i (\mathrm{i}\omega)^i}{1 + \sum_{i=1}^{n} \alpha_i (\mathrm{i}\omega)^i} \right] \tag{31}$$

Conclusion

This paper puts forward a dGMM method to predict the frequency-spatial attenuation of guided waves in anisotropic viscoelastic composite laminates by integrating the damping models (HR, KV, and BT) into the conventional pure elastic GMM. To efficiently solve the nonlinear transcendental DE, a two-step numerical algorithm is developed that combines the dGMM method, 2D MRCM, and the curve tracing technique. The proposed attenuation prediction approach is theoretically validated by comparing it with the SAFE method.

The energy velocities and attenuation coefficients at various frequencies are identified from recorded wave signals via the LR method which can not only process multiple sensing pairs necessarily for monitoring a practical aeronautic structure but also output statistical information such as the confidence interval and correlation coefficient R^2 to assess the quality of the identified parameters. With the experimental attenuation data, the unknown viscoelastic material properties are nondestructively estimated in the least square sense to achieve the best agreement of prediction to experimental data.

Experiments on two physically different structures, the homogeneous FCS and the inhomogeneous IFS with each one unmounted or mounted on an instrumented A380 plane, were carried out to experimentally validate the proposed dGMM approach. FCS is a slightly damped structure and IFS is highly damped. The existence of stress in the mounted case can greatly change the property of attenuation as compared to the unmounted case. To consider the

inhomogeneous characteristic of IFS, its core layer and skin layers are modeled by different damping models, thus two combinations of damping models (HR+BT and KV+BT) come into being. Both case studies demonstrate that the HR involved models predict more accurate attenuation than the KV involved models, and the spatial distribution of attenuation holds anisotropic property despite the quasi-isotropic stacking layups. In both structures, the A0 mode undergoes much attenuation than the S0 mode, thus selecting the S0 mode for SHM of similar aeronautic structures is desired if the dispersion aspect is not the determining factor.

In summary, using the actual and in-service data of the practical aeronautic structures to validate the proposed attenuation prediction method is not an easy task but makes it extremely valuable for the scientific and industrial communities. In this sense, this paper escorts the initiative of closing the gap between research and industrial deployment for SHM.[1]

Acknowledgments

The authors thank SAFRAN Nacelles for providing the unmounted A380 parts and AIRBUS for the authorization of bonding and data acquisition on their A380 test plane. Thanks also go to Prof. Zhenghua Qian and Dr Feng Zhu for their kind help during implementing the 2D MRCM.

Declaration of conflicting interests

The author(s) declared no potential conflicts of interest with respect to the research, authorship, and/or publication of this article.

Funding

The author(s) disclosed receipt of the following financial support for the research, authorship, and/or publication of this article: The first author is financially supported by the China Scholarship Council (CSC).

Notes

1. For notation homogeneity and for readability purposes, the frequency dependency is also shown for the HR model even if it is by definition frequency-independent.
2. It is possible to consider the complex frequency with real wavenumber. But this case does not relate to the wave propagation problem at hand.[21]
3. This property conforms with Snell's law[2] which requires that all the partial waves keep the same (complex) wavenumber in the interface between adjacent laminae along the wave propagation direction.

References

1. Cawley P. Structural health monitoring: closing the gap between research and industrial deployment. *Struct Health Monit* 2018; 17: 1225–1244.
2. Giurgiutiu V. *Structural health monitoring of aerospace composites*. London, UK: Elsevier Academic Press, 2015.
3. Su Z and Ye L. *Identification of damage using lamb waves: from fundamentals to applications*, Vol. 48. Berlin, Germany: Springer, 2009.
4. Wilcox P, Lowe M and Cawley P. The effect of dispersion on long-range inspection using ultrasonic guided waves. *NDT E Int* 2001; 34(1): 1–9.
5. Schubert KJ and Herrmann AS. On attenuation and measurement of lamb waves in viscoelastic composites. *Compos Struct* 2011; 94(1): 177–185.
6. Asamene K, Hudson L and Sundaresan M. Influence of attenuation on acoustic emission signals in carbon fiber reinforced polymer panels. *Ultrasonics* 2015; 59: 86–93.
7. Sreekumar P, Ramadas C, Anand A, et al. Attenuation of Ao lamb mode in hybrid structural composites with nanofillers. *Compos Struct* 2015; 132: 198–204.
8. Wilcox PD, Lowe MJS and Cawley P. Mode and transducer selection for long range lamb wave inspection. *J Intell Mater Syst Struct* 2001; 12(8): 553–565.
9. Rébillat M and Mechbal N. Damage localization in geometrically complex aeronautic structures using canonical polyadic decomposition of lamb wave difference signal tensors. *Struct Health Monit* 2020; 19(1): 305–321.
10. Haywood-Alexander M, Dervilis N, Worden K, et al. Structured machine learning tools for modelling characteristics of guided waves. *Mech Syst Signal Process* 2021; 156: 107628.
11. Gresil M and Giurgiutiu V. Prediction of attenuated guided waves propagation in carbon fiber composites using Rayleigh damping model. *J Intell Mater Syst Struct* 2015; 26(16): 2151–2169.
12. Treviso A, Van Genechten B, Mundo D, et al. Damping in composite materials: properties and models. *Compos B Eng* 2015; 78: 144–152.
13. Ramadas C, Balasubramaniam K, Hood A, et al. Modelling of attenuation of lamb waves using Rayleigh damping: numerical and experimental studies. *Compos Struct* 2011; 93(8): 2020–2025.
14. Mardanshahi A, Shokrieh MM and Kazemirad S. Simulated lamb wave propagation method for nondestructive monitoring of matrix cracking in laminated composites. *Struct Health Monit* 2021; 21: 695–709.
15. Zhu F, Wang B and Qian Z. A numerical algorithm to solve multivariate transcendental equation sets in complex domain and its application in wave dispersion curve characterization. *Acta Mech* 2019; 230(4): 1303–1321.
16. Cao X, Zeng L and Lin J. Lamb wave mode decomposition and reconstruction based on the viscoelastic propagation model. *Struct Health Monit* 2021; 20(1): 25–45.
17. Neau G. *Lamb waves in anisotropic viscoelastic plates: study of the wave fronts and attenuation*. PhD Thesis. Bordeaux, France: University of Bordeaux, 2003.
18. Zhu F, Wang B, Qian Z, et al. Accurate characterization of 3D dispersion curves and mode shapes of waves propagating in

generally anisotropic viscoelastic/elastic plates. *Int J Solids Struct* 2018; 150: 52–65.
19. Castaings M and Hosten B. Guided waves propagating in sandwich structures made of anisotropic, viscoelastic, composite materials. *J Acoust Soc Am* 2003; 113(5): 2622–2634.
20. Birgani PT, Sodagar S and Shishesaz M. Generation of low-attenuation lamb wave modes in three-layer adhesive joints. *Int J Acoust Vib* 2017; 22: 51–57.
21. Lowe MJS. Matrix techniques for modeling ultrasonic waves in multilayered media. *IEEE Trans Ultrason Ferroelectr Freq Control* 1995; 42(4): 525–542.
22. Dahmen S, Amor MB and Ghozlen MHB. Investigation of the coupled lamb waves propagation in viscoelastic and anisotropic multilayer composites by Legendre polynomial method. *Compos Struct* 2016; 153: 557–568.
23. Dahmen S and Glorieux C. Optimization of coupled lamb wave parameters for defect detection in anisotropic composite three-layer with Kelvin-Voigt viscoelasticity using Legendre polynomial method. *Compos Struct* 2021; 272: 114158.
24. Zhang X, Zhang C, Yu J, et al. Full dispersion and characteristics of complex guided waves in functionally graded piezoelectric plates. *J Intell Mater Syst Struct* 2019; 30(10): 1466–1480.
25. Calomfirescu M and Herrmann A. On the propagation of lamb waves in viscoelastic composites for SHM applications. *Key Eng Mater* 2007; 347: 543–548.
26. Torres-Arredondo MA and Fritzen CP. A viscoelastic plate theory for the fast modelling of lamb wave solutions in NDT/SHM applications. *Ultrasound* 2011; 66(2): 7–13.
27. Orta AH, Vandendriessche J, Kersemans M, et al. Modelling lamb wave propagation in visco-elastic composite plates using a fifth-order plate theory. *Ultrasonics* 2021; 116: 106482.
28. Manconi E and Mace BR. Estimation of the loss factor of viscoelastic laminated panels from finite element analysis. *J Sound Vib* 2010; 329(19): 3928–3939.
29. Manconi E and Sorokin S. On the effect of damping on dispersion curves in plates. *Int J Solids Struct* 2013; 50(11–12): 1966–1973.
30. Quintanilla FH, Fan Z, Lowe MJS, et al. Guided waves' dispersion curves in anisotropic viscoelastic single- and multi-layered media. *Proc Math Phys Eng Sci* 2015; 471(2183): 20150268.
31. Quintanilla FH, Lowe MJS and Craster RV. Full 3D dispersion curve solutions for guided waves in generally anisotropic media. *J Sound Vib* 2016; 363: 545–559.
32. Bartoli I, Marzani A, Di Scalea FL, et al. Modeling wave propagation in damped waveguides of arbitrary cross-section. *J Sound Vib* 2006; 295(3–5): 685–707.
33. Taupin L, Lhémery A and Inquiété G. A detailed study of guided wave propagation in a viscoelastic multilayered anisotropic plate. *J Phys Conf Ser* 2011; 269(1): 012002.
34. Mei H and Giurgiutiu V. Guided wave excitation and propagation in damped composite plates. *Struct Health Monit* 2019; 18(3): 690–714.
35. Shen Y and Cesnik CES. Hybrid local FEM/global LISA modeling of damped guided wave propagation in complex composite structures. *Smart Mater Struct* 2016; 25(9): 095021.
36. Shen Y and Cesnik CES. Local interaction simulation approach for efficient modeling of linear and nonlinear ultrasonic guided wave active sensing of complex structures. *J Nondestruct Eval Diagn Progn Eng Syst* 2018; 1(1): 1–9.
37. Ono K and Gallego A. Attenuation of lamb waves in CFRP plates. *J Acoust Emiss* 2012; 30: 109–123.
38. Margerit P, Lebée A, Caron JF, et al. The high-resolution wavevector analysis for the characterization of the dynamic response of composite plates. *J Sound Vib* 2019; 458: 177–196.
39. Fendzi C. *Structural health monitoring of composite structures: application to the monitoring of aeronautical nacelles*. PhD Thesis. Paris, France: ENSAM, 2015.
40. Rose JL. *Ultrasonic guided waves in solid media*. Cambridge, MA: Cambridge University Press, 2014.
41. Mastroddi F, Martarelli F, Eugeni M, et al. Time- and frequency-domain linear viscoelastic modeling of highly damped aerospace structures. *Mech Syst Signal Process* 2019; 122: 42–55.
42. Guo S, Rebillat M and Mechbal N. Dichotomy property of dispersion equation of guided waves propagating in anisotropic composite plates. *Mech Syst Signal Process* 2022; 164: 108212.
43. Wang L and Yuan FG. Group velocity and characteristic wave curves of Lamb waves in composites: modeling and experiments. *Compos Sci Technol* 2007; 67(7–8): 1370–1384.
44. Bernard A, Lowe MJS and Deschamps M. Guided waves energy velocity in absorbing and non-absorbing plates. *J Acoust Soc Am* 2001; 110(1): 186–196.
45. Tewary VK. Green's-function method for modeling surface acoustic wave dispersion in anisotropic material systems and determination of material parameters. *Wave Motion* 2004; 40(4): 399–412.
46. Boiko AV, Kulik VM, Seoudi BM, et al. Measurement method of complex viscoelastic material properties. *Int J Solids Struct* 2010; 47(3–4): 374–382.
47. Montalvão D, Cláudio R, Ribeiro AMR, et al. Experimental measurement of the complex Young's modulus on a CFRP laminate considering the constant hysteretic damping model. *Compos Struct* 2013; 97: 91–98.
48. Ramadas C. Three-dimensional modeling of lamb wave attenuation due to material and geometry in composite laminates. *J Reinf Plast Compos* 2014; 33(9): 824–835.
49. *Noliac piezoceramic material NCE51*, http://www.noliac.com/products/materials/nce51/ (2022, accessed 28 March 2022).
50. Yu L and Giurgiutiu V. Advanced signal processing for enhanced damage detection with piezoelectric wafer active sensors. *Smart Struct Syst* 2005; 1(2): 185–215.
51. Agrahari JK and Kapuria S. A refined Lamb wave time-reversal method with enhanced sensitivity for damage

detection in isotropic plates. *J Intell Mater Syst Struct* 2016; 27(10): 1283–1305.
52. Mei H and Giurgiutiu V. Effect of structural damping on the tuning between piezoelectric wafer active sensors and Lamb waves. *J Intell Mater Syst Struct* 2018; 29(10): 2177–2191.
53. Gandhi N, Michaels JE and Lee SJ. Acoustoelastic Lamb wave propagation in biaxially stressed plates. *J Acoust Soc Am* 2012; 132(3): 1284–1293.
54. Miao H and Li F. Shear horizontal wave transducers for structural health monitoring and nondestructive testing: a review. *Ultrasonics* 2021; 114: 106355.
55. Ledi KS, Hamdaoui M, Robin G, et al. An identification method for frequency dependent material properties of viscoelastic sandwich structures. *J Sound Vib* 2018; 428: 13–25.
56. Zhao J, Qiu J and Ji H. Reconstruction of the nine stiffness coefficients of composites using a laser generation based imaging method. *Compos Sci Technol* 2016; 126: 27–34.
57. Michaels JE and Michaels TE. Damage localization in inhomogeneous plates using a sparse array of ultrasonic transducers. *AIP Conf Proc* 2007; 894(1): 846–853.
58. Quaegebeur N, Masson P, Langlois-Demers D, et al. Dispersion-based imaging for structural health monitoring using sparse and compact arrays. *Smart Mater Struct* 2011; 20(2): 025005.
59. Balmes E and Leclère JM. *Viscoelastic vibration toolbox for use with MATLAB, user's guide version 1.0 [pdf]*. Online Referencing, http://www.sdtools.com/ (2017, accessed 28 March 2022).

Appendix 1

Polynomial coefficients in equation (12)

$$A_6 = C_{33}^* C_{44}^* C_{55}^* - C_{33}^* C_{45}^{*2} \tag{32}$$

$$\begin{aligned} A_4 = {} & \left(C_{44}^* C_{55}^* - C_{45}^{*2}\right)\left(C_{55}^* - \rho v^2\right) + C_{33}^* C_{55}^*\left(C_{66}^* - \rho v^2\right) \\ & + C_{33}^* C_{44}^*\left(C_{11}^* - \rho v^2\right) - 2C_{16}^* C_{45}^* C_{33}^* \\ & + 2\left(C_{36}^* + C_{45}^*\right)\left(C_{13}^* + C_{55}^*\right)C_{45}^* - \left(C_{13}^* + C_{55}^*\right)^2 C_{44}^* \\ & - \left(C_{45}^* + C_{36}^*\right)^2 C_{55}^* \end{aligned} \tag{33}$$

$$\begin{aligned} A_2 = {} & C_{33}^*\left(C_{11}^* - \rho v^2\right)\left(C_{66}^* - \rho v^2\right) \\ & + C_{44}^*\left(C_{11}^* - \rho v^2\right)\left(C_{55}^* - \rho v^2\right) \\ & + C_{55}^*\left(C_{66}^* - \rho v^2\right)\left(C_{55}^* - \rho v^2\right) \\ & - \left(C_{11}^* - \rho v^2\right)\left(C_{45}^* + C_{36}^*\right)^2 \\ & - \left(C_{66}^* - \rho v^2\right)\left(C_{13}^* + C_{55}^*\right)^2 - 2\left(C_{55}^* - \rho v^2\right)C_{16}^* C_{45}^* \\ & + 2C_{16}^*\left(C_{45}^* + C_{36}^*\right)\left(C_{13}^* + C_{55}^*\right) - C_{16}^{*2} C_{33}^* \end{aligned} \tag{34}$$

$$A_0 = \left[\left(C_{11}^* - \rho v^2\right)\left(C_{66}^* - \rho v^2\right) - C_{16}^{*2}\right]\left(C_{55}^* - \rho v^2\right) \tag{35}$$

Appendix 2

Abbreviations

2D MRCM	2D Module Ratio Convergence Method
BT	Biot damping model
CFRP	Carbon fiber reinforced polymer
DAS	Digital acquisition system
DE(s)	Dispersion equation(s)
ESPRIT	Estimation of signal parameters via rotational invariance techniques
FCS	Fan cowl structure
(d)GMM	(damped) Global matrix method
HR	Hysteretic damping model
IFS	Inner fixed structure
KV	Kelvin–Voigt damping model
LISA	Local interaction simulation approach
LR	Linear regression method
PWSA	Partial wave superposition approach
PZT(s)	Piezoelectric transducer(s)
RAPID	Reconstruction algorithm for probabilistic inspection of defects
SAFE	Semi-analytical finite element method
SCM	Spectral collocation method
SHM	Structural health monitoring
TMM	Transfer matrix method
ToA	Time of arrival
WFEM	Wave finite element method